Monthly Notices
of the
ROYAL ASTRONOMICAL SOCIETY

Mon. Not. R. Astron. Soc. **423,** 1089–1108 (2012) doi:10.1111/j.1365-2966.2012.20935.x

AMI radio continuum observations of young stellar objects with known outflows⋆

AMI Consortium: Rachael E. Ainsworth,[1]† Anna M. M. Scaife,[2] Tom P. Ray,[1] Jane V. Buckle,[3,4] Matthew Davies,[3] Thomas M. O. Franzen,[5] Keith J. B. Grainge,[3,4] Michael P. Hobson,[3] Natasha Hurley-Walker,[6] Anthony N. Lasenby,[3,4] Malak Olamaie,[3] Yvette C. Perrott,[3] Guy G. Pooley,[3] John S. Richer,[3,4] Carmen Rodríguez-Gonzálvez,[7] Richard D. E. Saunders,[3,4] Michel P. Schammel,[3] Paul F. Scott,[3] Timothy Shimwell,[5] David Titterington[3] and Elizabeth Waldram[3]

[1]*Dublin Institute for Advanced Studies, 31 Fitzwilliam Place, Dublin 2, Ireland*
[2]*School of Physics & Astronomy, University of Southampton, Highfield, Southampton SO17 1BJ*
[3]*Astrophysics Group, Cavendish Laboratory, J J Thomson Avenue, Cambridge CB3 0HE*
[4]*Kavli Institute for Cosmology, Cambridge, Madingley Road, Cambridge CB3 0HA*
[5]*CSIRO Astronomy & Space Science, Australia Telescope National Facility, PO Box 76, Epping, NSW 1710, Australia*
[6]*International Centre for Radio Astronomy Research, Curtin Institute of Radio Astronomy, 1 Turner Avenue, Technology Park, Bentley, WA 6845, Australia*
[7]*Spitzer Science Center, MS 220-6, California Institute of Technology, Pasadena, CA 91125, USA*

Accepted 2012 March 15. Received 2012 March 14; in original form 2012 February 10

ABSTRACT

We present 16 GHz (1.9 cm) deep radio continuum observations made with the Arcminute Microkelvin Imager (AMI) of a sample of low-mass young stars driving jets. We combine these new data with archival information from an extensive literature search to examine spectral energy distributions (SEDs) for each source and calculate both the radio and sub-mm spectral indices in two different scenarios: (1) fixing the dust temperature ($T_{\rm d}$) according to evolutionary class; and (2) allowing $T_{\rm d}$ to vary. We use the results of this analysis to place constraints on the physical mechanisms responsible for the radio emission. From AMI data alone, as well as from model fitting to the full SED in both scenarios, we find that 80 per cent of the objects in this sample have spectral indices consistent with free–free emission. We find an average spectral index in both $T_{\rm d}$ scenarios, consistent with free–free emission. We examine correlations of the radio luminosity with bolometric luminosity, envelope mass and outflow force, and find that these data are consistent with the strong correlation with envelope mass seen in lower luminosity samples. We examine the errors associated with determining the radio luminosity and find that the dominant source of error is the uncertainty on the opacity index, β. We examine the SEDs for variability in these young objects, and find evidence for possible radio flare events in the histories of L1551 IRS 5 and Serpens SMM 1.

Key words: radiation mechanisms: general – stars: formation – ISM: clouds – ISM: general.

1 INTRODUCTION

Young stellar objects (YSOs) are divided into a number of evolutionary classes. Class 0 protostars represent the youngest phase of protostellar evolution (André, Ward-Thompson & Barsony 1993) in which the protostar has yet to accrete most of its mass from the surrounding envelope, and therefore the central object is less massive than the envelope ($M_{\rm env} > M_*$). The subsequent Class I phase (Lada 1987) occurs when a majority of the remainder of the envelope has accreted on to the protostar or its circumstellar disc ($M_{\rm env} < M_*$). The Class II phase (Lada 1987), also known as the Classical T Tauri stage, occurs when infall is almost complete and the central object is embedded in an optically thick disc and enters the pre-main-sequence (PMS) stage of evolution. Embedded YSOs are

⋆ We request that any reference to this paper cites 'AMI Consortium: Ainsworth et al. 2012'.

†E-mail: rainsworth@cp.dias.ie

often found to have partially ionized and collimated outflows/jets driven by the accretion from their envelopes, and are detectable from molecular gas tracers such as CO and by the shocks along the length of the outflows. The outflows driven by Class I protostars are less powerful than those of Class 0 due to a decline in the accretion rate (Bontemps et al. 1996).

The target sample in this work comprises Class 0 and Class I protostars. Since the mass ratio $M_{\rm env} > M_*$ is not directly observable, André et al. (1993), André, Ward-Thompson & Barsony (2000) define the following observational properties required to identify an object as Class 0. The first is the detection of a compact centimetre radio continuum source, a collimated CO outflow, or an internal heating source as indirect evidence for a central YSO. These criteria distinguish the central object from a starless prestellar core. The second requirement is centrally peaked but extended submillimetre continuum emission tracing the presence of a spheroidal circumstellar dust envelope (as opposed to just a disc). The third is a high ratio of submillimetre to bolometric luminosity, corresponding to an envelope mass greater than the stellar mass. Class 0 spectral energy distributions (SEDs) are typically well characterized by single temperature blackbodies with $15 \leq T_{\rm d} \leq 30\,{\rm K}$ and where $T_{\rm d}$ is the dust temperature. The second and third criteria differentiate Class 0 sources from the more evolved Class I and II objects. For further distinction, bolometric temperature is also used to characterize evolutionary class, where $T_{\rm bol} < 70\,{\rm K}$ for Class 0 objects and $70 < T_{\rm bol} < 650\,{\rm K}$ for Class I (Chen et al. 1995).

The radio counterpart at centimetre wavelengths for these low-mass young stars is detected almost certainly via thermal bremsstrahlung radiation. This 'free-free' emission is typically observed to be compact and elongated along the outflow axis, leading to the designation of these sources as 'thermal radio jets' (e.g. Rodríguez 1995). Free–free emission at these wavelengths typically has a flat or positive power-law spectral index α, where the flux density $S_\nu \propto \nu^\alpha$ at frequency ν. It has been shown that $\alpha = 0.6$ for a standard conical jet, and $\alpha < 0.6$ for an unresolved, partially opaque flow where the cross-sectional area grows more slowly than length (Reynolds 1986; Anglada et al. 1998). However, in a number of cases non-thermal emission is also seen (e.g. Ray et al. 1997; Carkner et al. 1997; Feigelson, Carkner & Wilking 1998; Carrasco-González et al. 2010a). There are some objects that have yielded spectral indices too negative to be explained by free–free emission alone, such as the Serpens MMS 1 triple radio source (Rodríguez et al. 1989b; Curiel et al. 1993; AMI Consortium: Scaife et al. 2012b), suggesting that non-thermal processes must contribute. The radio emission can also be attributed, at least at very short wavelengths, to the discs around these young stars (Rodríguez et al. 2008b).

Here we present 16 GHz observations of a sample of classic low-mass young stars driving outflows. These sources are selected to match the target sample for the e-MERLIN (extended Multi-Element Radio Linked Interferometer Network) legacy project at 5 GHz on the morphology and time evolution of thermal jets associated with low-mass young stars (P.I. Rodríguez). The high spatial resolution observations provided by the e-MERLIN programme will resolve out the larger scale emission from these objects and only detect the small-scale localized emission from the central source and shocks along the length of their collimated outflows. In contrast, the data presented here will not resolve the separate components of the radio emission but will measure the integrated radio emission from these objects. This *total* radio emission at 16 GHz from YSOs has been demonstrated to show clearly defined trends with the other global properties of these systems, such as bolometric luminosity, envelope mass and outflow force (AMI Consortium: Scaife et al. 2011a,b, 2012b). If such free–free emission is to be reconciled with ionization mechanisms arising from the impact of the molecular outflow or protostellar jet/wind on its surroundings then it is vital to measure it in its entirety to determine quantitatively its physical correspondence to other global properties of the protostellar system, in much the same way that radio emission from massive YSOs can be used to infer the total ionizing flux of the central object and hence its spectral type. Such indirect measures of protostellar activity in the early embedded phase of YSO lifetimes may provide a window into the evolution of these objects, which is otherwise obscured.

In this paper we investigate the properties of the integrated radio emission from this sample of low-mass YSOs. In general, these new data confirm trends found in previous works and improve upon the statistics. We identify outliers which may provide useful targets for further study at high spatial resolution. We combine our results for the flux densities with those found in an extensive literature search to calculate the spectral indices at radio wavelengths, and which are overwhelmingly consistent with free–free emission as the mechanism for the radio emission.

This paper is organized as follows. In Section 2 we describe the sample of targets to be observed. In Section 3 we describe the AMI telescope, the observations and the data reduction process. In Section 4 we comment on the results of the observations, and Section 5 contains detailed notes on the individual fields. In Section 6 we discuss the detections and non-detections, the expected contamination from extragalactic sources, the SEDs, the radio spectral indices, the derivation of physical parameters, correlations between the radio luminosity and other global properties, and, finally, evidence for variability. We make concluding remarks in Section 7.

2 THE SAMPLE

This study targets 11 YSOs driving known outflows. The coordinates of each of these objects are listed in Columns 3 and 4 of Table 1 along with their identifier. We follow the classification scheme described in Hatchell et al. (2007a) for Class 0 or Class I protostars, based on three evolutionary indicators, which for a Class I are $T_{\rm bol} > 70\,{\rm K}$, $L_{\rm bol}/L_{\rm smm} > 3000$ and $F_{3.6}/F_{850} > 0.003$, where $F_{3.6}$ is the flux at 3.6 cm and F_{850} is the flux at 850 μm. There are eight Class 0 and three Class I protostars in the target sample, listed in Table 1. A number of additional sources were detected within the AMI fields. We identify these additional sources assuming a generous threshold of 10 arcsec of a known protostellar source to allow for low signal-to-noise ratio; however the maximum offset is found to be <4 arcsec. Additional sources are listed in Table 2. When combined with the original target list, these additional sources will be referred to as the 'extended sample'. For the purposes of this work, all other detected sources are considered to be extragalactic and this is discussed further in Section 6. Physical properties of the sources including parent cloud association, distance, bolometric temperature, bolometric luminosity, envelope mass and outflow force are listed in Table 3. We note that the bolometric luminosities of the target sample span an order of magnitude, and the range of envelope masses places the sample in the intermediate to high end of the range for PMS stars.

A number of the physical properties listed in Table 3 depend on the distance to the source. For example, many studies assume a distance to Perseus of 320 pc (e.g. Hatchell et al. 2007a), but here we assume a distance of $D = 250\,{\rm pc}$ in order to remain consistent with the *Spitzer* 'Cores to Disks' (c2d) catalogue of deeply embedded protostars (Dunham et al. 2008). Values in the literature also

Table 1. Sample selection. Column 1 contains the source name; 2 the protostellar evolutionary class as defined by our criteria described in Section 2; 3 the Right Ascension in units of hours, minutes and seconds; 4 the Declination in units of degrees, minutes and seconds; 5 the date the observation was made, 6 AMI flux calibrator; 7 AMI phase calibrator; 8 rms noise measured from recovered map; 9 major axis of AMI synthesized beam and 10 minor axis of AMI synthesized beam.

Source	Class	RA (J2000)	Dec. (J2000)	Date (yyyy-mm-dd)	1°	2°	$\sigma_{\rm rms}$ (μJy beam^{-1})	$b_{\rm maj}$ (arcsec)	$b_{\rm min}$ (arcsec)
L1448 IRS 3	0	03 25 36.49	+30 45 22.0	2010-09-23	3C48	J0324+3410	24	41.8	27.4
HH 7-11	I	03 29 03.73	+31 16 03.8	2010-09-24	3C48	J0324+3410	26	40.2	28.2
L1551 IRS 5	I	04 31 34.15	+18 08 04.8	2010-09-30	3C48	J0428+1732	24	50.9	27.2
L1527	0	04 39 53.87	+26 03 09.9	2010-09-25	3C48	J0440+2728	19	44.3	28.4
HH 1-2 MMS 1	0	05 36 22.85	−06 46 06.6	2010-10-12	3C48	J0541−0541	61	70.5	24.0
HH 26 IR	I	05 46 03.90	−00 14 52.5	2011-08-27	3C48	J0558+0044	34	78.0	28.5
HH 111	0	05 51 46.25	+02 48 29.7	2010-10-06	3C48	J0552+0313	31	68.7	27.4
NGC 2264 G	0	06 41 11.05	+09 55 59.2	2010-10-04	3C48	J0654+1004	33	54.5	26.9
Serpens MMS 1	0	18 29 49.79	+01 15 20.8	2010-10-11	3C48	J1824+0119	36	66.5	25.7
L723	0	19 17 53.67	+19 12 19.6	2010-09-30	3C48	J1914+1636	23	48.1	26.3
L1251 A	0	22 35 24.95	+75 17 11.4	2010-09-25	3C147	J2236+7322	25	37.6	27.8

Table 2. Additional detected sources. Column 1 contains the additional source number; 2, the field the source is located in; 3–4, the Right Ascension and Declination of the peak flux value; 5, the AMI 16 GHz combined channel flux density; 6, the spectral index $\alpha_{\rm AMI}$ calculated from the AMI fluxes; 7, the associated source and 8, the protostellar evolutionary class where applicable or object type.

AMI source	Field	RA (J2000)	Dec. (J2000)	$S_{16\,\rm GHz}$ (mJy)	$\alpha_{\rm AMI}$	Associated source	Class
1	L1448	03 25 38.9	+30 44 02	0.76 ± 0.09	-0.67 ± 0.98	L1448 C	0
2	HH 7-11	03 28 55.5	+31 14 35	0.39 ± 0.10	1.84 ± 0.16	NGC 1333 *IRAS* 2A	0
3	HH 7-11	03 28 57.3	+31 14 16	0.50 ± 0.10	1.65 ± 0.34	NGC 1333 *IRAS* 2B	I
4	L1551	04 31 44.3	+18 08 29	0.74 ± 0.09	0.61 ± 0.75	L1551 NE	0
5	L1527	04 39 49.4	+26 05 25	0.96 ± 0.09	-0.10 ± 0.92	HH 192 VLA 2	Ext?
6	L1527	04 39 59.8	+26 02 06	0.88 ± 0.09	-1.25 ± 0.58	HH 192 VLA 3	Ext?
7	HH 1-2	05 36 25.7	−06 47 16	1.00 ± 0.26	0.10 ± 1.10	HH 2	HH
8	HH 26 IR	05 46 07.4	−00 13 42	1.23 ± 0.10	1.82 ± 0.13	HH 25 MMS	0
9	HH 111	05 51 45.5	+02 50 06	0.70 ± 0.15	-0.23 ± 1.10	–	Ext?
10	L1251	22 35 20.5	+75 19 44	0.71 ± 0.09	-1.20 ± 0.68	–	Ext?

differ for the distance to the Taurus and Orion molecular clouds, and the values we adopt, along with their references, are listed in Table 3. Physical quantities from the literature have been adjusted for distance where necessary.

3 OBSERVATIONS

The data in this work were taken with the Arcminute Microkelvin Imager (AMI) Large Array at the Mullard Radio Astronomy Observatory near Cambridge, UK (AMI Consortium: Zwart et al. 2008). AMI comprises eight 13-m dishes, operating between 13.5 and 17.9 GHz with eight 0.75 GHz bandwidth channels. The channels 1–3 were not used due to a poorer response in this frequency range and interference due to geostationary satellites. The full width at half-maximum (FWHM) of the primary beam of the AMI is ≈6 arcmin at 16 GHz.

AMI data reduction is performed using the local software tool REDUCE. This applies both automatic and manual flags for interference, shadowing and hardware errors. REDUCE Fourier transforms the lag correlator data to synthesize frequency channels and performs phase and amplitude calibration before output to disc in *uv* FITS format. Flux (primary) calibration is performed using 3C48 for all fields except for L1251 where 3C147 was used, and assumed flux densities can be found in Table 4. Phase (secondary) calibration is carried out using the bright point sources listed in Table 1. Absolute calibration is typically accurate to 5 per cent but we note that an increased absolute calibration error of 10 per cent is applied to flux densities from channel 8 in order to reflect the poorer phase stability of this channel relative to the others.

Reduced data were imaged in CASA.[1] Multiple data sets were concatenated; additional baseline flagging was carried out and the CLEAN task was used for deconvolution to produce the combined frequency image as well as the separate spectral channel images. Primary beam correction and fitting Gaussian models to radio sources in order to extract flux densities were performed in AIPS.[2] All errors quoted are 1σ.

4 RESULTS

Maps were made using naturally weighted visibilities to ensure optimal signal-to-noise ratio levels, except in the case of HH 1-2 in which uniform weighting was used to improve resolution. As HH 1-2 is the lowest-declination source, the beam would otherwise have been very extended. The dimensions of the synthesized beam for each source are listed in Table 1. Source detection for these data was performed in the un-primary-beam-corrected maps, where

[1] http://casa.nrao.edu
[2] http://aips.nrao.edu

Table 3. Source information. Column 1 contains the source name, 2, the molecular cloud association; 3, the distance to the source; 4, distance reference; 5, bolometric temperature; 6, bolometric luminosity; 7, reference for $T_{\rm bol}$ and $L_{\rm bol}$; 8, envelope mass calculated using the 850 μm flux from the Fundamental Map Object Catalogue (di Francesco et al. 2008); 9, outflow force of the source and 10, reference for the outflow force of the source.

Source	Cloud association	D (pc)	d Ref.	$T_{\rm bol}$ (K)	$L_{\rm bol}$ ($L_\odot$)	Ref.	$M_{\rm env}$ ($M_\odot$)	$F_{\rm out}$ ($M_\odot^{-5}$ km s^{-1} yr^{-1})	$F_{\rm out}$ Ref.
L1448 IRS 3	Perseus	250	1	53	13.7	6	16.22	$49.9 \times 10^{-2} \pm 5.29$	12
HH 7-11	Perseus	250	1	180	18.0	6	10.75	1.53 ± 18.0	12
L1551 IRS 5	Taurus	140	2	75	15.3	7	6.22	9.63	13
L1527	Taurus	140	2	59	2.0	8	5.89	0.79 ± 0.13	17
HH 1-2 MMS 1	Orion	420	3	–	23	9	42.46	–	–
HH 26 IR	Orion	420	3	–	25.1	10	4.68	36.1	13
HH 111	Orion	420	3	49	19.2	11	13.90	4.57	13
NGC 2264 G	Mon OB1	800	4	25	12	4	11.59	300	13
Serpens MMS 1	Serpens	260	14	56	17.3[a]	15	28.17	2.8	16
L723	–	300	4	50	3	4	5.14	26	13
L1251 A	Cepheus Flare	320	5	–	2.24	5	14.83	8.6	13
L1448 C	Perseus	250	1	49	3.9	6	5.1	$16.3 \times 10^{-2} \pm 1.9$	12
NGC 1333 *IRAS* 2A	Perseus	250	1	58	13.9	6	2.81[b]	$56.8 \times 10^{-2} \pm 5.6$	12
NGC 1333 *IRAS* 2B	Perseus	250	1	106	5.3	15	0.74[b]	–	–
L1551 NE	Taurus	140	2	56	4.2	11	5.6	–	–
HH 25 MMS	Orion	420	3	34	5.2	4	43.96	–	–

References: (1) Dunham et al. (2008); (2) Kenyon, Dobrzycka & Hartmann (1994); (3) Menten et al. (2007); (4) André et al. (2000); (5) Kun et al. (2009); (6) Hatchell et al. (2007a); (7) van Kempen et al. (2009); (8) Jørgensen et al. (2009); (9) Fischer et al. (2010); (10) Nisini, Giannini & Lorenzetti (2002); (11) Froebrich (2005); (12) Hatchell, Fuller & Richer (2007b); (13) Anglada (1995); (14) Straižys, Černis & Bartašiūtė (1996); (15) Enoch et al. (2009b); (16) Graves et al. (2010); (17) Bontemps et al. (1996).
[a] Enoch et al. (2009a).
[b] Enoch et al. (2009b).

Table 4. AMI frequency channels and primary calibrator flux densities measured in Jy.

Channel no.	4	5	6	7	8
Freq. (GHz)	14.62	15.37	16.12	16.87	17.62
3C48	1.75	1.66	1.58	1.50	1.43
3C147	2.62	2.50	2.40	2.30	2.20

we identified all objects within the FWHM of the AMI primary beam with a peak flux density $>5\sigma_{\rm rms}$, where $\sigma_{\rm rms}$ is the rms noise determined from the maps. $\sigma_{\rm rms}$ for each target field is listed in Table 1. Integrated flux densities for detected sources were then extracted from the primary-beam-corrected maps using IMFIT and are listed in Table 5. The errors on the flux densities are calculated as $\sigma = \sqrt{(0.05S_\nu)^2 + \sigma_{\rm fit}^2 + \sigma_{\rm rms}^2}$, where $\sigma_{\rm fit}$ is the fitting error returned from IMFIT and $0.05S_\nu$ is a conservative 5 per cent absolute

Table 5. Integrated flux densities. Column 1 contains the source name; 2, the combined-channel 16 GHz flux density for that source; 3–7 contain the AMI integrated flux densities for each source from AMI channels 4–8, and 8 contains the spectral index $\alpha_{\rm AMI}$ calculated from the AMI fluxes.

Source	$S_{16\,\rm GHz}$ (mJy)	AMI channel number 4 [14.62 GHz] (mJy)	5 [15.37 GHz] (mJy)	6 [16.12 GHz] (mJy)	7 [16.87 GHz] (mJy)	8 [17.62 GHz] (mJy)	$\alpha_{\rm AMI}$
L1448 IRS 3	2.39 ± 0.16	2.40 ± 0.25	2.34 ± 0.26	2.41 ± 0.37	2.26 ± 0.24	2.62 ± 0.37	0.20 ± 0.73
HH 7-11	3.63 ± 0.24	3.43 ± 0.20	3.10 ± 0.18	3.91 ± 0.22	3.43 ± 0.19	3.83 ± 0.41	0.70 ± 0.41
L1551 IRS 5	4.97 ± 0.27	4.74 ± 0.25	4.37 ± 0.24	4.79 ± 0.28	4.82 ± 0.29	5.48 ± 0.57	0.79 ± 0.40
L1527	1.33 ± 0.10	1.04 ± 0.11	1.04 ± 0.14	1.12 ± 0.12	1.20 ± 0.16	1.38 ± 0.19	1.15 ± 0.57
HH 1-2 MMS 1	1.70 ± 0.27	1.30 ± 0.28	1.53 ± 0.30	1.34 ± 0.18	1.33 ± 0.14	–	-0.17 ± 1.02
HH 26 IR	0.39 ± 0.08	–	–	–	–	–	–
HH 111	2.49 ± 0.20	3.11 ± 0.53	2.68 ± 0.28	2.39 ± 0.26	2.86 ± 0.30	2.51 ± 0.40	-0.40 ± 0.85
NGC 2264 G	0.30 ± 0.22	–	–	–	–	–	–
Serpens MMS 1	7.32 ± 0.41	8.21 ± 0.77	7.66 ± 0.55	7.04 ± 0.43	6.77 ± 0.44	7.30 ± 0.83	-0.73 ± 0.56
L723	0.58 ± 0.09	0.58 ± 0.09	0.52 ± 0.06	0.65 ± 0.08	0.66 ± 0.07	0.52 ± 0.11	0.42 ± 0.82
L1251 A	1.05 ± 0.12	0.86 ± 0.18	0.98 ± 0.14	1.00 ± 0.20	0.76 ± 0.16	1.10 ± 0.25	0.06 ± 0.99

calibration error (except for channel 8 where we use a 10 per cent absolute calibration error, $0.1S_\nu$). Including $\sigma_{\rm fit}$ provides an overestimation to the total error.

Extracted flux densities are listed in Table 5, and Column 8 of Table 5 lists the spectral indices $\alpha_{\rm AMI}$ calculated over the AMI channels. The uncertainties of these values are large due to the short frequency coverage of AMI. Spectral indices are discussed further in Section 6. In two cases, HH 26 IR and NGC 2264, the flux density was extracted only from the 16 GHz combined-channel image. For these objects, the flux density in the combined-channel image is $< 5\sqrt{n}\sigma$, where n is the number of combined channels, indicating that the sources would be detected at $<5\sigma$ in the individual channel maps. Combined-channel maps for each source may be found in Appendix A with the exception of L1448 IRS 3 which is shown in Fig. 1(a) for illustration purposes.

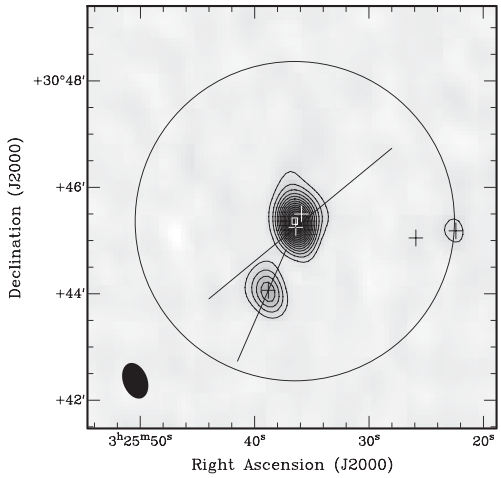

(a)

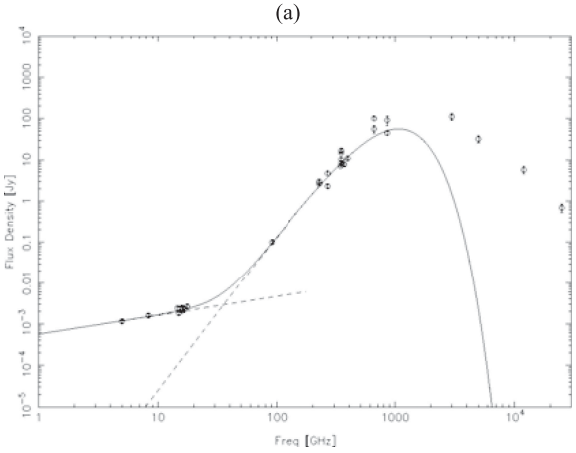

(b)

Figure 1. L1448. (a) The AMI 16 GHz combined channel map uncorrected for the primary beam response for L1448. The positions of known Class 0 and Class I objects are indicated as crosses (+) and are from Hatchell et al. (2007a). The solid black lines indicate outflow axes for L1448 NB (northern axis) and L1448 C (southern axis) from Wolf-Chase et al. (2000) (details are given in Section 5). We plot the half power point of the primary beam as a solid circle (≈6 arcmin at 16 GHz) and the FWHM of the PSF as the filled ellipse in the bottom-left corner (see Table 1). Contours at 5, 10, 15, $20\,\sigma_{\rm rms}$, etc., where $\sigma_{\rm rms} = 24\,\mu{\rm Jy\,beam^{-1}}$. (b) The SED for L1448 IRS 3 with the observed radio spectra over the AMI frequency channels 3–8 combined with flux densities from the literature.

5 NOTES ON INDIVIDUAL FIELDS

L1448. L1448 IRS 3 is made up of the L1448 North group of Class 0 protostars, NA, NB and NW (Curiel et al. 1990; Terebey & Padgett 1997). AMI does not resolve the separate sources, so the data at 1.9 cm (see Fig. 1a) represent the integrated radio emission from the three protostars and appear point-like. The SED of this source is shown in Fig. 1(b), and includes the observed radio spectra over the AMI frequency channels 3–8 combined with flux densities from the literature. SEDs and spectral indices are discussed in Section 6.

L1448 NA and NB are in a 7 arcsec separation protobinary system (Curiel et al. 1990) and L1448 NW lies approximately 20 arcsec north-west of L1448 NA (Terebey & Padgett 1997) in the Perseus molecular cloud. The outflows in this region have been discussed extensively by Wolf-Chase et al. (2000). Only redshifted gas associated with the outflow of L1448 NA is detected in their CO maps, with a PA (measured from north through east) of ≈150° and a total length of at least 0.7 pc (at their assumed distance of 300 pc). The outflow associated with L1448 NB has a PA ≈ 129° and 6 arcmin to the north-west along the outflow axis lie the blueshifted optical emission knots of HH 196 (Bally et al. 1997); the directions of these outflows are illustrated in Fig. 1(a).

We also detect L1448 C in our map, which is the driving source of the high velocity outflow in L1448 (Bachiller et al. 1990). The blueshifted CO outflow lobe driven by L1448 C begins with a PA = 159° (Bachiller et al. 1995) (see Fig. 1a) before being deflected through a total angle of ≈32° due to a possible collision with the core containing L1448 NA and NB (Davis & Smith 1995; Curiel et al. 1999).

HH 7-11. The AMI 1.9 cm data presented here (see Fig. A1) show emission extended in a direction almost perpendicular to the direction of the HH 7-11 outflow, but consistent with the distribution of Very Large Array (VLA) objects of Rodríguez, Anglada & Curiel (1999), almost all of which are associated with YSOs.

HH 7-11 SVS 13 is a designated Class I object in NGC 1333 within the Perseus molecular cloud, and is generally believed to be the driving source of the chain of HH 7-11 knots to the southeast. However, using high-resolution VLA data Rodríguez, Anglada & Curiel (1997) propose that VLA 3, detected ∼6 arcsec southwest of SVS 13 (VLA 4), is instead the driving source of the HH 7-11 outflow. VLA 3 is better aligned with the HH 7-11 knots and the elongation of the source is approximately along the axis of the Herbig–Haro (HH) and molecular flows. Rodríguez et al. (1997) suggest that SVS 13 is the driving source of a much smaller, nearby chain of HH objects to the east.

We also detect NGC 1333 *IRAS* 2A and 2B in our map, which were first detected by Jennings et al. (1987) as *IRAS* 2, and subsequently by Sandell et al. (1994) who detected a quadrupolar outflow centred on the source suggesting that it might be a binary. The two sources, *IRAS* 2A and 2B, were detected at 3.6 and 6 cm by Rodríguez et al. (1999) (VLA 7 and 10, respectively) who suggest that the quadrupolar outflow may originate from *IRAS* 2A and which therefore itself may be a binary.

L1551. L1551 IRS 5 is a deeply embedded multiple protostellar Class I source in Taurus that drives a binary jet (Rodríguez et al. 2003a). At 1.9 cm (see Fig. A1) this source appears point-like and it has been suggested that the emission for this source near 1 cm arises from nearly equal contributions of dust emission from the discs and free–free emission from the ionized ejecta (Rodríguez 1998).

Rodríguez et al. (2003b) have shown that the emission at centimetre wavelengths is produced by a pair of closely aligned (within

≈12°) bipolar ionized jets, which themselves are aligned with the larger scale bipolar molecular outflow. Lim & Takakuwa (2006) determined that L1551 IRS 5 is a triple protostellar system by identifying two main (N and S) components, separated by ≃0.3 arcsec, each comprising a circumstellar dust disc and bipolar ionized jet, and a third component lying ≈0.09 arcsec southeast of the N component as another circumstellar dust disc.

We detect, but do not resolve, the Class 0 source L1551 NE (Moriarty-Schieven, Butner & Wannier 1995) to the east of IRS 5 at 1.9 cm. L1551 NE has a molecular outflow and is likely to drive the HH objects 28, 29 and 454 (Devine, Reipurth & Bally 1999). Radio continuum observations at 3.5 cm identified L1551 NE as a binary source with separation 0.5 arcsec (Reipurth et al. 2002).

L1527. We detect L1527 (IRAS 04368+2557) at 1.9 cm as a point source (see Fig. A1). This object is an embedded Class 0 (Melis et al. 2011) protostar in the Taurus molecular cloud with a compact accretion disc and a ≈0.2 arcsec binary companion (Loinard et al. 2002). The HH 192 outflow associated with this object has an east–west orientation (Gomez, Whitney & Kenyon 1997) with an edge-on disc perpendicular to the outflow axis (Tobin, Hartmann & Loinard 2010) that is infalling on to the central source (Ohashi et al. 1997). AMI Consortium: Scaife et al. (2012a) found an opacity index $\beta = 0.32 \pm 0.04$ for this source, consistent with the presence of large dust grains, or *pebbles*, in the disc.

We also detect HH 192 VLA 2 and 3 (Rodríguez & Reipurth 1998) at 1.9 cm; there are no other references to these objects in the literature. We find a spectral index of $\alpha_{\rm AMI} = -0.10$ for VLA 2 consistent with optically thin free–free emission and $\alpha_{\rm AMI} = -1.25$ for VLA 3 which is inconsistent with free–free emission and suggests that it could be extragalactic. For the purposes of this work, VLA 2 and 3 are considered to be extragalactic sources (see Section 6) although the emission from VLA 2 could be consistent with an H II region.

HH 1-2. At 1.9 cm, we detect the HH 1-2 outflow driving source as a point source (see Fig. A1). HH 1 and 2 are considered to be the prototypes of the HH phenomena, displaying two bright bow shocks which expand as a part of a bipolar outflow moving away from the central source that drives a finely collimated jet (Rodríguez et al. 2000). The Class 0 driving source of HH 1 and 2, VLA 1, was detected as a centimetre continuum radio source by Pravdo et al. (1985), and subsequent observations have shown that the source powers a small thermal radio jet along the axis of the HH flow (Rodríguez et al. 1990). Another source, VLA 2, was found 3 arcsec from VLA 1, producing the HH 144 flow which is at a large angle to the HH 1 flow axis. The AMI does not resolve the two sources VLA 1 and 2 and the combined thermal emission is approximately point-like.

The Herbig–Haro objects HH 1 and HH 2 themselves have been previously detected at centimetre wavelengths (e.g. Rodríguez et al. 1990, 2000) and we detect HH 2 but we do not detect HH 1 at 1.9 cm. Rodríguez et al. (1990) find a flux density of 0.78 mJy at 2 cm for HH 1; however we constrain an upper flux density limit of 0.34 mJy, suggesting that this source is variable. Radio continuum emission from other HH objects has been found to be time variable (Rodríguez et al. 2008a; Carrasco-González et al. 2010b). Rodríguez et al. (1990) find flux densities of 1.75 mJy for the central source and 0.98 mJy for HH 2, for which our data are consistent.

HH 26 IR. HH 26 IR is a weak source at 1.9 cm (see Fig. A1), a Class I protostar (Davis et al. 1997) located within L1630 in Orion that drives a molecular outflow.

L1630 is rich in star formation activity and has a complex morphology. Two embedded Class 0 protostars, HH 24MMS and HH 25MMS, are also in this star formation region and both have compact jets, while the outflow of HH 26 IR drives a more extended outflow (Gibb & Heaton 1993). H_2 knots HH 26A, B, C and D exist along the axis of the HH 26 IR outflow which is approximately orthogonal to the HH 25 outflow (Davis et al. 1997). We also detect HH 25 MMS within the AMI primary beam to the northeast of HH 26 IR.

HH 111. At 1.9 cm, HH 111 (see Fig. A1) is significantly extended along an approximate north–south direction, perpendicular to the known outflow direction. The driving source is IRAS 05491+0247, a suspected Class I binary source (Yang et al. 1997) that drives a bipolar molecular outflow. The outflow was first discovered in the optical by Reipurth (1989). However, based on the classification criterion defined in Section 2, this source has a bolometric temperature consistent with a Class 0 object and this is discussed further in Section 6. The jet is well-collimated, aligned approximately in the E–W direction, and has knots with velocities ranging from 300 to 600 km s^{-1} for different parts of the jet complex (Reipurth, Raga & Heathcote 1992). It was found that the optical jet is part of a giant HH complex extending over 7.7 pc (Reipurth, Bally & Devine 1997).

Near-infrared observations (Gredel & Reipurth 1994) revealed a second bipolar flow, HH 121, emerging from around the same position as the optical outflow and is aligned approximately in the N–S direction, consistent with the extension observed here. Such a quadrupolar outflow is indicative of a binary companion. 3.6 cm (Reipurth et al. 1999) and 7 mm (Rodríguez et al. 2008b) VLA observations suggest a common origin within ≈0.1 arcsec. It has been suggested that the most viable interpretations for the structure are that the observations are of two orthogonal discs around separate protostars or a disc with a perpendicular jet (Rodríguez et al. 2008b).

NGC 2264. We detect emission from NGC 2264 G at $9\sigma_{\rm rms}$ in the AMI combined-channel map (see Fig. A2). The NGC 2264 G molecular outflow was one of nine discovered in a CO survey of the Monoceros OB1 cloud conducted by Margulis & Lada (1986) and was found to have very high velocity emission and a well-collimated, bipolar morphology (Margulis, Lada & Snell 1988). It is centred on IRAS 06384+0958 and extends ≈1.6 pc in an approximately E–W direction (Caratti o Garatti et al. 2006). Lada & Fich (1996) show that the outflow is S-shaped and symmetric with respect to the driving source, VLA 2, which was detected by Gómez et al. (1994) using VLA ammonia observations. They obtained a spectral index for the outflow of $\alpha \simeq 0.3 \pm 0.2$ which is consistent with optically thin free–free emission of a thermal jet, and their 3.6 cm VLA images show VLA 2 to be elongated in the direction of the outflow. Subsequent observations of VLA 2 by Ward-Thompson, Eiroa & Casali (1995) using the James Clerk Maxwell Telescope (JCMT) obtained a ratio of submillimetre and bolometric luminosity indicative of a Class 0 protostar.

Serpens. At 1.9 cm, AMI does not resolve the triple radio source SMM 1 but measures the integrated radio emission. The emission is oriented in an approximate N–S direction (see Fig. A2), despite the outflow orientation of NW–SE which could be due to the presence of multiple objects in this region. The Serpens molecular cloud is a nearby star formation region containing clusters of low-mass protostars as well as several HH objects and outflows. The most luminous and most deeply embedded object in the Serpens cloud core is the triple radio source SMM 1, comprising a central source, a NW component, and a SE component, and is a known Class 0 source

associated with a highly collimated radio continuum jet (Rodríguez et al. 1989b).

Curiel et al. (1993) presented high-sensitivity, multi-frequency VLA radio continuum observations of the triple radio source, showing a one-sided radio jet morphology, but did not detect a counter jet. These authors show that the central source is extended at 3.6 cm, but the difference between the direction of the major axis and the orientation of the radio jet appears to be significant, suggesting that the central source is precessing or nutating. They find that the central source has a spectral index $\alpha \simeq 0.15 \pm 0.09$, consistent with the value of $\alpha \simeq 0.1 \pm 0.1$ obtained by Rodríguez et al. (1989b), while the NW and SE components have spectral indices $\alpha \simeq -0.05 \pm 0.05$ and $\alpha \simeq -0.30 \pm 0.04$, respectively. These results suggest a thermal origin for the emission associated with the central source and the NW component, and a borderline thermal/non-thermal origin for the SE component. AMI Consortium: Scaife et al. (2012b) present evidence for radio variability in SMM 1, as previously suggested by Enoch et al. (2009a) who detect a high-mass disc around the source. Here, we adopt a bolometric luminosity of $L_{\rm bol} = 17.3\,{\rm L}_{\odot}$ (Enoch et al. 2009a); however we note that significantly higher luminosities have been reported for this object (e.g. $46\,{\rm L}_{\odot}$ from Hurt & Barsony 1996).

L723. L723, also known as IRAS 19156+1906, appears point-like at 1.9 cm (see Fig. A2). L723 is a designated low-mass, Class 0 object (Lee et al. 2002). The associated outflow consists of a pair of bipolar lobes aligned along the east–west direction and another pair of bipolar lobes aligned roughly in the north–south direction, with IRAS 19156+1906 located at their common centre (Lee et al. 2002). VLA observations at 3.6 cm reveal two sources, VLA 1 and VLA 2, towards the centre of the outflow (Anglada et al. 1991), although VLA 1 is likely a background source (Anglada, Rodríguez & Torrelles 1996; Girart et al. 1997). VLA 2 has a jet-like morphology and partially optically thick free–free emission, characteristic of a thermal radio jet, and was first identified as the powering source of the EW pair of molecular lobes by Anglada et al. (1996). Recent VLA observations by Carrasco-González et al. (2008) at 3.6 cm and 7 mm resolve VLA 2 into several components and the two brightest sources at 3.6 cm, VLA 2A and 2B, are separated by ≈0.29 arcsec.

L1251. The emission at 1.9 cm of L1251 A is detected as a point source (see Appendix A). L1251 A is a star-forming region towards Cepheus, and is centred on the bright source IRAS 22343+7501 which is associated with a large-scale (∼10 arcmin) molecular outflow (Schwartz, Gee & Huang 1988; Sato & Fukui 1989). VLA observations (Meehan et al. 1998; Beltrán et al. 2001; Reipurth et al. 2004a) show several radio sources (VLA 6, 7 and 10) within this region that could possibly drive the molecular outflow. Reipurth et al. (2004a) show two sources with clear extension, VLA 7 and 10, and suggest that VLA 10 could drive the molecular outflow found by Sato & Fukui (1989), which extends for 10 arcmin in the approximate NE–SW direction. However, VLA 7 is consistent with the outflow found by Schwartz et al. (1988) that has an outflow direction in an almost perpendicular direction, and the emission we detect is consistent with this. We do not resolve these sources, but measure the integrated radio emission.

6 DISCUSSION

6.1 Detections and non-detections

We detect 100 per cent of the objects in the target sample with AMI at 16 GHz, which includes eight Class 0 and three Class I protostars based on the classification scheme described in Section 2. We also detect five additional Class 0 and one additional Class I sources within the AMI primary beam of these fields, all of which are Class 0 sources driving outflows except for NGC 1333 *IRAS* 2B which is Class I.

Table 6. Summary of detection statistics. The original sample includes only objects listed in Table 1. The extended sample includes all objects listed in Tables 1 and 2, inclusive of the original sample.

Class	Present	Detected	per cent
Original Sample:			
Class 0	8	8	100
Class I	3	3	100
Extended Sample:			
Class 0	15	12	80
Class I	7	4	57

In the L1448 field there is one Class 0 source (31; Hatchell et al. 2007a) that we do not detect, in the HH 7-11 field there is one Class 0 (62; Hatchell et al. 2007a) and one Class I (50; Hatchell et al. 2007a) that we do not detect, and in the Serpens field there is one Class 0 (VLA 5; AMI Consortium: Scaife et al. 2012b) and two Class I (VLA 9, 16; AMI Consortium: Scaife et al. 2012b) sources that we do not detect.

We identify AMI 7 as the radio counterpart to HH 2, but we do not detect HH 1 at 1.9 cm even though it has been previously detected at centimetre wavelengths. We also do not detect any HH 192 objects in the L1527 field which lie within the AMI primary beam.

Detection statistics for the original and extended samples divided by evolutionary class are listed in Table 6. It is not surprising that we should detect 100 per cent of the target sample as all sources have been previously detected at centimetre wavelengths and have known radio jets. Detection rates for Class 0 in the extended sample is typical compared to AMI Consortium: Scaife et al. (2011b, 2012b) but high for Class I. This is likely due to the small sample size or the fact that a majority of the extended sample consists of the original sample which was chosen on the basis that these objects have been detected at these wavelengths before. The original sample is biased, and for these reasons it is difficult to draw strong statistical conclusions from this sample.

6.2 Expected contamination by extragalactic radio sources

At 16 GHz we expect a certain number of extragalactic radio sources to be seen within each of our fields. Following AMI Consortium: Scaife et al. (2011a,b, 2012b), to quantify this number we use the 15 GHz source counts model from de Zotti et al. (2005) scaled to the 10C survey source counts (AMI Consortium: Davies et al. 2011). The average rms noise from our data sets is $\backsimeq 30\,\mu$Jy beam^{-1} and from this model we predict that we should see 0.043 sources arcmin^{-2}, or $\backsimeq 2$ radio sources within a 6 arcmin FWHM primary beam above a $5\sigma_{\rm rms}$ flux density of 150 μJy. Accounting for the radial attenuation of the primary beam, we would therefore expect to see $\approx 10 \pm 3$ extragalactic radio sources within our target fields. Making the assumption that all sources which cannot be identified with a previously known protostellar object are extragalactic we find four radio sources, lower than predicted but consistent at the 2σ level. The low number of extragalactic sources detected in these fields compared to the model may represent an overestimation from the 15 GHz source counts, which are extrapolated from a

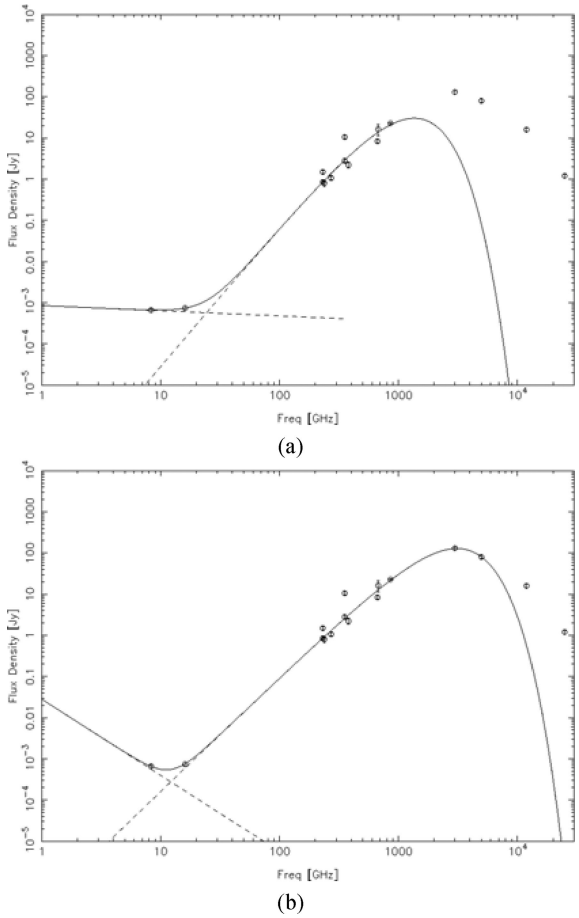

Figure 2. The SED fits for L1551 NE when (a) $T_{\rm d} = 15$ K, and (b) when $T_{\rm d}$ is allowed to vary. In the first case, the method determines α' for the two low-frequency data points, but in the second case the AMI data point is fit as greybody emission and α' is unconstrained.

completeness limit of 0.5 mJy and is high compared with our detection limit of 0.15 mJy. One break in the observed source counts is already known at mJy flux density levels (AMI Consortium: Davies et al. 2011) and it is possible that a further break exists below 0.5 mJy.

6.3 Spectral energy distributions

An extensive literature search was conducted for unresolved, integrated flux densities to include in the SEDs. It should be noted that Wendker (1995) was a useful reference. High-resolution data that were highly discrepant due to flux loss or data with high uncertainties (e.g. 450 μm data from di Francesco et al. 2008) were not included. SEDs are shown in Figs 1(b), 2, B1–B3 with maximum likelihood models (see Table 8) overlaid. The list of archival data used in the SEDs can be found in Appendix C. Where uncertainties were not provided, an error of 10 per cent was used in the model fittings and this is indicated by a dagger symbol (†) in Appendix C. Only data $\nu < 3$ THz ($\lambda > 100$ μm) were included in the fit, but *IRAS* data $\nu > 3$ THz are included in the plots for illustration.

6.3.1 Maximum likelihood SED fitting

Power-law spectral indices, $\alpha_{\rm AMI}$, were fitted to the AMI channel data alone for each object (see Tables 2 and 5), using the Markov chain Monte Carlo based Maximum Likelihood algorithm METRO (Hobson & Baldwin 2004). The fit is of the form:

$$S_\nu \propto \nu^{\alpha_{\rm AMI}}, \tag{1}$$

where S_ν is the flux density measured at frequency ν.

METRO was then used to fit a combined radio power law, with spectral index α', and blackbody model to the larger data set for each source. This fit utilized data at wavelengths longer than 100 μm and had the form:

$$S_{\rm total} = S_1 + S_2 = K_1 \left(\frac{\nu}{\nu_1}\right)^{\alpha'} + K_2 \frac{\nu^\beta B_\nu(T_{\rm d})}{\nu_2^\beta B_{\nu_2}(T_{\rm d})}, \tag{2}$$

where β is the dust opacity index, B_ν is the Planck function for a dust temperature $T_{\rm d}$, K_1 is the normalized flux density at $\nu_1 = 16$ GHz and K_2 is the normalized flux density at $\nu_2 = 300$ GHz. Fitting was performed in two scenarios to obtain the maximum likelihood values for the spectral index α' of each source. These two scenarios are as follows.

(i) fixing the dust temperature based on evolutionary class,
(ii) allowing the dust temperature to vary.

It can be seen that when $\nu = \nu_1$, S_1 equals K_1, the normalized flux density at 16 GHz and when $\nu = \nu_2$, S_2 equals K_2, the normalized flux density at 300 GHz, and we define these parameters as $S_{16}^{\rm norm}$ and $S_{300}^{\rm norm}$, respectively. We use uniform and separable priors for all parameters, with ranges

$$\Pi = \Pi_\alpha(-2, 2)\Pi_\beta(0, 3)\Pi_{T_{\rm d}}(5, 45). \tag{3}$$

6.3.2 The greybody contribution

When $\nu = \nu_1 = 16$ GHz, the free–free component should dominate the total flux density; however at 16 GHz there is also expected to be a small contribution to the radio flux density of protostars due to the long wavelength tail of the thermal dust emission from the envelopes around these objects (e.g. AMI Consortium: Scaife et al. 2012a).

It is important to separate the greybody component from the free–free emission and we calculate this predicted contribution to the 16 GHz flux density in the following way:

$$S_{\rm gb,16} = f(K_2, \beta, T_{\rm d}) = K_2 \frac{\nu^\beta B_{16}(T_{\rm d})}{\nu_2^\beta B_{300}(T_{\rm d})}, \tag{4}$$

with an associated error

$$\sigma_{S,16}^2 = \left(\frac{\partial f}{\partial K_2}\sigma_{K_2}\right)^2 + \left(\frac{\partial f}{\partial \beta}\sigma_\beta\right)^2 + \left(\frac{\partial f}{\partial T_{\rm d}}\sigma_{T_{\rm d}}\right)^2, \tag{5}$$

where $\nu = 16$ GHz, $\nu_2 = 300$ GHz, and σ_{K_2}, σ_β and $\sigma_{T_{\rm d}}$ are the uncertainties on K_2, β and $T_{\rm d}$ respectively, and listed in Tables 7 and 8. In all cases, we find that the error, $\sigma_{S,16}$, is dominated by the uncertainty on β. For example, in the case of L1448: $\sigma_{S,16}^2 = 4.39^2 \pm 75.8^2 \pm 14.3^2$ μJy.

We subtract the value of $S_{\rm gb,16}$ from the measured 16 GHz flux density to remove the contribution of thermal dust emission and obtain values of only the radio emission due to the outflow component at 16 GHz, $S_{\rm rad,16}$. This is to ensure that the values used do not include contributions from the thermal dust tail which varies greatly between sources and which might therefore influence any conclusions being drawn from the correlations examined in a later section of this paper. We compute the radio luminosity $S_{\rm rad,16}D^2$ using the greybody-subtracted radio flux densities and the distance values listed in Table 3 to use in the correlations in Section 6.6. If the

Table 7. Model results for fixed T_d. Column 1 contains the source name; 2, the spectral index; 3, the opacity index; 4, the dust temperature, where 15 K was used for Class 0 sources and 20 K for Class I; 5, the normalized flux density at 16 GHz; 6, the normalized flux density at 300 GHz; 7, the predicted greybody contribution at 16 GHz and 8, the radio luminosity measured at 16 GHz with the predicted thermal dust contribution subtracted. 'UC' is used to indicate that the parameter is unconstrained.

Source	α'	β	T_d (K)	S_{16}^{norm} (mJy)	S_{300}^{norm} (Jy)	$S_{gb,16}$ (μJy)	$S_{rad,16}D^2$ (mJy kpc^2)
L1448 IRS 3	0.37 ± 0.09	1.48 ± 0.05	15	1.88 ± 0.09	4.96 ± 0.15	297.47 ± 52.50	0.131
HH 7-11	1.12 ± 0.04	1.92 ± 0.02	20	3.03 ± 0.08	5.30 ± 0.19	77.96 ± 4.83	0.222
L1551 IRS 5	0.10 ± 0.04	1.52 ± 0.14	20	3.90 ± 0.17	4.47 ± 0.43	214.58 ± 130.38	0.093
L1527	0.17 ± 0.08	0.96 ± 0.10	15	0.85 ± 0.05	0.49 ± 0.02	134.94 ± 52.75	0.023
HH 1-2 MMS 1	0.23 ± 0.04	2.38 ± 0.08	15	1.49 ± 0.07	0.99 ± 0.02	4.33 ± 1.25	0.299
HH 26 IR	UC	0.62 ± 0.07	20	0.04 ± 0.06	0.56 ± 0.03	372.00 ± 101.97	–
HH 111	0.88 ± 0.07	1.66 ± 0.07	15	2.16 ± 0.09	0.90 ± 0.02	31.95 ± 8.81	0.434
NGC 2264 G	-0.29 ± 0.24	1.44 ± 0.39	15	0.50 ± 0.10	0.54 ± 0.65	37.06 ± 192.75	–
Serpens MMS 1	-0.06 ± 0.02	1.47 ± 0.05	15	6.89 ± 0.14	5.22 ± 0.20	327.71 ± 56.62	0.473
L723	-0.26 ± 0.09	1.83 ± 0.07	15	0.58 ± 0.03	0.93 ± 0.05	20.04 ± 5.15	0.050
L1251 A	1.79 ± 0.15	2.92 ± 0.27	15	0.91 ± 0.07	0.32 ± 0.07	0.29 ± 0.51	0.107
L1448 C	1.12 ± 0.12	2.10 ± 0.04	15	0.53 ± 0.02	1.64 ± 0.04	16.25 ± 2.41	0.046
NGC 1333 *IRAS* 2A	2.42 ± 0.07	2.01 ± 0.05	15	0.43 ± 0.02	1.52 ± 0.10	19.33 ± 3.67	0.023
NGC 1333 *IRAS* 2B	1.31 ± 0.05	1.95 ± 0.09	20	1.02 ± 0.04	0.53 ± 0.04	7.16 ± 2.69	0.031
L1551 NE	-0.13 ± 0.31	1.41 ± 0.03	15	0.60 ± 0.09	1.83 ± 0.02	136.09 ± 11.08	0.012
HH 25 MMS	2.13 ± 0.04	1.68 ± 0.16	15	0.97 ± 0.07	0.83 ± 0.10	27.82 ± 22.30	0.212

Table 8. Model results for variable T_d. Column 1 contains the source name; 2, the spectral index; 3, the opacity index; 4, the dust temperature; 5, the normalized flux density at 16 GHz; 6, the normalized flux density at 300 GHz; 7, the predicted greybody contribution at 16 GHz and 8, the radio luminosity measured at 16 GHz with the predicted thermal dust contribution subtracted. 'UC' is used to indicate that the parameter is unconstrained.

Source	α'	β	T_d (K)	S_{16}^{norm} (mJy)	S_{300}^{norm} (Jy)	$S_{gb,16}$ (μJy)	$S_{rad,16}D^2$ (mJy kpc^2)
L1448 IRS 3	0.46 ± 0.09	1.81 ± 0.12	10.77 ± 0.95	2.02 ± 0.09	5.13 ± 0.12	145.74 ± 77.31	0.140
HH 7-11	1.28 ± 0.04	3.00 ± 0.08	12.53 ± 0.90	3.24 ± 0.07	6.21 ± 0.27	4.92 ± 1.59	0.227
L1551 IRS 5	0.09 ± 0.03	1.46 ± 0.05	26.74 ± 2.07	$3.87 \pm 0.0.09$	4.54 ± 0.17	233.58 ± 43.54	0.093
L1527	0.20 ± 0.08	0.81 ± 0.11	44.86 ± 1.57	0.86 ± 0.06	0.44 ± 0.03	138.81 ± 60.00	0.023
HH 1-2 MMS 1	0.21 ± 0.04	2.18 ± 0.19	16.93 ± 1.80	1.46 ± 0.07	1.01 ± 0.02	7.35 ± 7.38	0.299
HH 26 IR	UC	0.66 ± 0.16	17.36 ± 5.25	0.04 ± 0.09	0.59 ± 0.04	368.59 ± 300.38	–
HH 111	0.84 ± 0.07	1.55 ± 0.17	17.33 ± 3.68	2.11 ± 0.10	0.90 ± 0.02	41.31 ± 35.89	0.366
NGC 2264 G	-0.31 ± 0.11	1.71 ± 0.13	18.30 ± 1.88	0.49 ± 0.06	0.36 ± 0.02	10.02 ± 5.59	0.186
Serpens	-0.07 ± 0.02	1.25 ± 0.04	28.54 ± 1.54	6.74 ± 0.14	4.85 ± 0.18	451.87 ± 71.01	0.464
L723	-0.29 ± 0.09	1.59 ± 0.13	17.56 ± 1.31	0.56 ± 0.04	0.92 ± 0.04	37.73 ± 20.70	0.049
L1251 A	1.70 ± 0.14	2.27 ± 0.41	20.85 ± 4.36	0.86 ± 0.07	0.38 ± 0.06	1.98 ± 7.84	0.107
L1448 C	1.17 ± 0.15	2.22 ± 0.11	12.70 ± 1.25	0.54 ± 0.03	1.69 ± 0.04	12.88 ± 5.99	0.047
NGC 1333 *IRAS* 2A	2.56 ± 0.03	2.76 ± 0.19	9.85 ± 1.10	0.46 ± 0.02	1.17 ± 0.07	2.22 ± 2.20	0.024
NGC 1333 *IRAS* 2B	1.40 ± 0.05	2.89 ± 0.26	9.55 ± 1.90	1.06 ± 0.03	0.57 ± 0.06	0.76 ± 1.28	0.031
L1551 NE	UC	0.78 ± 0.05	40.64 ± 3.29	0.17 ± 0.07	1.69 ± 0.02	585.75 ± 0.05	–
HH 25 MMS	UC	0.55 ± 0.09	41.27 ± 3.65	0.004 ± 0.18	1.51 ± 0.09	1021.76 ± 352.26	–

greybody subtracted flux density is not distinct from zero by $>3\sigma$, we consider the radio luminosity consistent with zero (see Tables 7 and 8).

6.3.3 Comparison of the two scenarios

In Scenario (i), the algorithm was run by fixing T_d to 15 K for Class 0 objects and to 20 K for Class I objects, and allowing the other parameters to vary to determine their maximum likelihood values. Overall, fixing the dust temperature provided reasonable fits to the SEDs, with the exception of L1527, NGC 2264 G, Serpens MMS 1, and L1551 NE where it provided a poor fit to the greybody peaks. The results for the maximum likelihood values of α', β, S_{16}^{norm} and S_{300}^{norm} in each case are listed in Table 7, along with the dust temperature used (Columns 2–6), the greybody contribution at 16 GHz (Column 7) and the radio luminosity at 16 GHz with the greybody contribution subtracted out (Column 8). We find a weighted average spectral index of $\overline{\alpha'} = 0.20 \pm 0.41$ for the original sample, consistent with free–free emission, and a dust opacity index of $\overline{\beta} = 1.75 \pm 0.36$. Quoted errors represent the standard deviation of the distribution of values, rather than the standard error on the mean.

In Scenario (ii), we do not fix T_d and allow the algorithm to determine the maximum likelihood value for this parameter along with α', β, S_{16}^{norm} and S_{300}^{norm}. The results for these parameters along with $S_{gb,16}$ and $S_{rad,16}D^2$ are listed in Table 8. We again find a weighted average spectral index of $\overline{\alpha'} = 0.20 \pm 0.46$ for the original sample consistent with free–free emission. We find an opacity index of $\overline{\beta} = 1.52 \pm 0.56$ and a dust temperature $\overline{T_d} = 18.46 \pm 9.77$ for the original sample.

In the first scenario, with fixed T_d, 80 per cent of the sources in the original sample for which the spectral indices could be constrained had maximum likelihood values of $2 > \alpha' > -0.1$, consistent with free–free emission. In the second scenario, with T_d varying, again 80 per cent of the sources in the original sample had α' consistent with free–free emission. In both cases, NGC 2264 G and L723 have spectral indices that are inconsistent with free–free emission and $\alpha' < -0.1$, suggesting non-thermal emission. The one source for which an accurate value of α' is unconstrained in the original sample is HH 26 IR, due to insufficient low-frequency data. Unconstrained parameters are indicated in Tables 7 and 8 by 'UC'. Since α' is unconstrained for HH 26 IR, the algorithm attributes all the flux density at 16 GHz to thermal dust emission, resulting in a value of $S_{rad,16}D^2 \approx 0$ when subtracted from the AMI flux density. Consequently, it does not appear in the correlations in Section 6.6.

A spectral index of $\alpha > 2$ is generally considered unphysical for free–free emission, and is attributed to dust emission. In the cases where the likelihood distribution pushed the upper limit of the prior range, we increased the prior range to $\Pi_\alpha(-2, 3)$. In the extended sample, NGC 1333 *IRAS* 2A has $\alpha' > 2$ in both model scenarios, suggesting that the lower frequency data are an extension of the greybody emission and that there is no free–free component. This will not be reflected accurately in the calculation of the greybody emission at 16 GHz since the algorithm constrains a separate α' component, and this will in turn affect the radio luminosity calculated for this source and the correlations discussed in Section 6.6. When T_d is fixed (Scenario i), HH 25 MMS also has $\alpha' > 2$, suggesting that it is purely greybody emission. This will have the same consequences as for NGC 1333 *IRAS* 2A. However, α' is unconstrained for HH 25 MMS when T_d is allowed to vary (Scenario ii) and this will have the reverse effect on the radio luminosity. Examining the SED plot (see Appendix B), it is possible that HH 25 MMS has a free–free component based on one or two data points, but the model is unable to constrain it without more low-frequency data.

For L1551 NE, α' is constrained in Scenario (i) but not in Scenario (ii). Consequently, the calculated radio luminosities differ significantly between the two scenarios and this will affect the correlations in Section 6.6. Specifically, $S_{rad,16}d^2$ is a factor of 4.3 higher when T_d is allowed to vary than when it is fixed to 15 K (see Tables 7 and 8). When T_d is fixed for this source, the peak of the greybody is constrained by the given dust temperature (and does not fit the higher frequency data), allowing the algorithm to determine α' using the two low-frequency data points (see Fig. 2a). However, when T_d is allowed to vary, the AMI data point at 16 GHz is fit as part of the greybody emission and α' is left unconstrained, as there is only one remaining low-frequency data point (see Fig. 2b). This results in a more significant greybody contribution at 16 GHz. Therefore the radio luminosity will be significantly lower when $S_{gb,16}$ is subtracted in this scenario compared to that when the dust temperature is fixed, and this will drastically change its position on the correlation plots between the two scenarios. The same situation is also found in the case of HH 25 MMS.

6.4 Dust temperatures

In Scenario (ii), where T_d varies, our results for T_d range between 9 and 45 K. Values in the literature for the dust temperatures associated with Class 0 and I sources are found to range between 10 and 40 K (Reipurth et al. 1993; Dent, Matthews & Ward-Thompson 1998; Shirley, Evans & Rawlings 2002; Young et al. 2003; Hatchell et al. 2007a). Dent et al. (1998) find that their sample of Class 0 protostars can be fitted with optically thin emission, a β index between 1 and 1.5, and a dust temperature between 20 and 30 K. These authors derive for their Class I sources β between 1 and 2 and a dust temperature of 30 K, of which our results are consistent.

For Class 0 sources, we find weighted average values of $\overline{\beta} = 1.35 \pm 0.29$ and $\overline{T_d} = 20.1 \pm 10.89$, and for Class I sources we find $\overline{\beta} = 1.81 \pm 0.74$ and $\overline{T_d} = 14.85 \pm 5.15$. These results are reversed from what we expect based on the first SED scenario, but this is likely to be due to the low number of Class I sources in our sample compared to Class 0. AMI Consortium: Scaife et al. (2012a) find $\beta = 0.3$ for L1527 by fitting data from 5 to 350 GHz jointly using the sum of two power laws, which is slightly shallower than the value of $\beta = 0.81 \pm 0.11$ found in this work. However, both are consistent with the value of $\beta \leq 1$, indicating the presence of large dust grains.

6.5 Radio spectral indices

Typically, the radio emission detected at centimetre wavelengths for Class 0 and I protostars is observed to possess a flat or rising spectrum, indicating that it occurs as a consequence of free–free radiation from ionized gas. Unresolved sources can exhibit partially opaque spectra with spectral indices in the range $-0.1 \leq \alpha \leq 2$, where a value of -0.1 indicates optically thin free–free emission and a value of 2 indicates optically thick. For the case of a standard, canonical jet with constant opening angle, the spectral index $\alpha = 0.6$. Shallower spectral indices ($\alpha < 0.6$) are expected for unresolved, well-collimated, ionized outflows, and steeper spectra still ($\alpha > 0.9$) are expected for fully ionized, adiabatic jets (Reynolds 1986). In this section we compare our results for α_{AMI} (Tables 2 and 5) and α' from the SED scenario where T_d is allowed to vary (Table 8).

Across the AMI band, 7/9 (78 per cent) of the target sources, where the spectral index α_{AMI} could be constrained, are within the range $-0.1 \leq \alpha_{AMI} \leq 2$ indicating free–free emission (see Table 5). When including the additional protostellar sources detected in these fields, 11/14 (79 per cent) of the sources have α_{AMI} within this range. The three sources that lie outside this range, HH 111, Serpens and L1448 C, have $\alpha_{AMI} < -0.1$, typically indicating that another emission mechanism is at work. However, spectral indices inconsistent with free–free emission have been found previously for Serpens MMS 1 (Rodríguez et al. 1989b; Curiel et al. 1993). The weighted average spectral index of the original sample calculated from the AMI fluxes is $\overline{\alpha_{AMI}} = 0.42 \pm 0.59$, consistent with a canonical jet. The flux densities for HH 26 IR and NGC 2264 could only be extracted from the 16 GHz combined-channel map, so it was not possible to measure α_{AMI} for these sources. For the extended sample, $\overline{\alpha_{AMI}} = 1.52 \pm 0.64$, still consistent with free–free emission. The large uncertainties of α_{AMI} in Table 5 are due to the short frequency coverage of AMI.

For comparison, 8/10 (80 per cent) of the original sample have $-0.1 \leq \alpha' \leq 2$ when including archival data (again, excluding HH 26 IR, see Table 8). For the extended sample, 10/13 (77 per cent) of

the sources (excluding L1551 NE and HH 25 MMS) have α' within this range. The values for α' that lie outside this range are NGC 2264 and L723 ($\alpha' < -0.1$) and NGC 1333 *IRAS* 2A ($\alpha' > 2$). The original sample has a weighted average spectral index $\overline{\alpha'} = 0.20 \pm 0.46$ and the extended sample has $\overline{\alpha'} = 0.37 \pm 0.63$, both consistent with free–free emission and a well-collimated flow.

In the case of NGC 2264 G, there are two known radio continuum sources in this outflow region: VLA 1, which was proposed as the driving source by Rodríguez & Curiel (1989), and VLA 2, which is suggested to be the driving source by Gómez et al. (1994). Gómez et al. (1994) find a spectral index $\alpha \simeq -1.3 \pm 0.4$ for VLA 1 and a significantly lower flux density than Rodríguez & Curiel (1989), suggesting that it appears to be highly variable and an extragalactic nature cannot be ruled out. For VLA 2, these authors find a spectral index $\alpha \simeq 0.3 \pm 0.2$, consistent with free–free emission. The negative spectral index $\alpha' = -0.31 \pm 0.11$ obtained here for NGC 2264 G is likely contaminated by VLA 1 as the sources are unresolved by AMI. Additional high-resolution observations are needed to confirm the non-thermal component.

L723 is in a similar situation to NGC 2264 G, where there is a nearby source, VLA 1, with spectral index $\alpha \leq -0.1$ that could be contaminating the results in the SED for the prospective driving source, VLA 2. Anglada et al. (1996) find a spectral index $\alpha = -0.3 \pm 0.2$ for VLA 1, and discuss the possibility that the source is a radio-emitting, optically obscured T Tauri star. These authors find a spectral index $\alpha = 0.5 \pm 0.2$ for VLA 2, consistent with free–free emission, and the results of Carrasco-González et al. (2008) for the spectral index of VLA 2 are also indicative of free–free emission. We find $\alpha_{\rm AMI} = 0.42 \pm 0.82$ for L723, consistent with free–free emission from a canonical jet even though we do not resolve these sources. The negative spectral index $\alpha' = -0.29 \pm 0.09$ we obtain is likely affected by both VLA 1 and insufficient low-frequency data to better constrain α'.

From the data presented here, L1527 is found to have a spectral index $\alpha_{\rm AMI} = 1.15 \pm 0.57$, which agrees with the value of $\alpha_{\rm AMI} = 1.17 \pm 0.42$ found by AMI Consortium: Scaife et al. (2012a). A spectral index of $\alpha > 0.8$ can be easily produced by velocity gradients or the recombination that might be expected for rapidly diverging flows (Reynolds 1986). For consistency purposes, we have used the same archival data as in AMI Consortium: Scaife et al. (2012a) for the SED, who find $\alpha' = -0.11 \pm 0.09$. However, we find $\alpha' = 0.70 \pm 0.06$ in this work. We attribute this difference to the fact that the data are fitted with multiple greybody components in AMI Consortium: Scaife et al. (2012a). L1527 has a known disc (Loinard et al. 2002; Tobin et al. 2010) which dominates the SED at sub-mm frequencies, while the envelope contribution dominates at far-infrared frequencies. The single greybody model used in this work does not provide the best fit to both the envelope and disc. However, in both scenarios the SED model here predicts $\beta \leq 1$, consistent with the presence of large dust grains in the disc (AMI Consortium: Scaife et al. 2012a).

Overall, the values for the spectral indices are consistent as all sources listed in Table 5 and the protostellar sources listed in Table 8 have known outflows. In the cases of NGC 2264 G and L723, higher spatial resolution data can help constrain the emission mechanism for the driving sources of these outflows and identify non-thermal components.

6.6 Correlations

Radio luminosity has been shown to correlate with global properties such as bolometric luminosity, envelope mass and outflow force

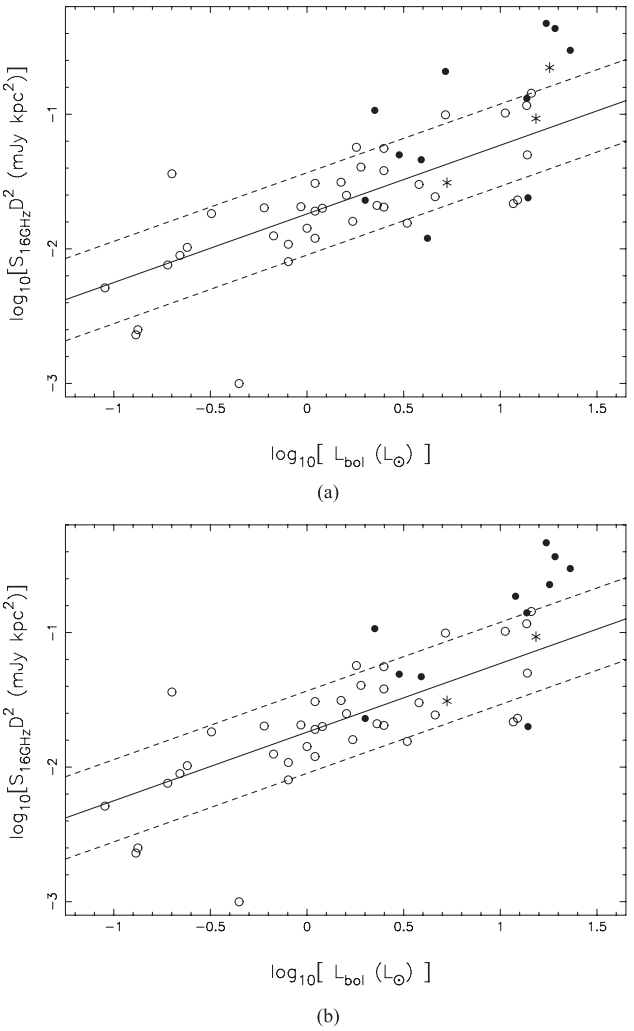

Figure 3. (a) Correlation of bolometric luminosity with 1.9 cm radio luminosity when $T_{\rm d}$ is fixed, and (b) correlation of bolometric luminosity with 1.9 cm radio luminosity when $T_{\rm d}$ varies. Filled circles represent Class 0 sources from this sample, stars are Class I, and unfilled circles are previous data. Best-fitting correlations from AMI Consortium: Scaife et al. (2011b) are shown as solid lines.

(AMI Consortium: Scaife et al. 2011a,b, 2012b). We do not repeat these discussions here, but combine our data with the previous work to redraw the correlations (see Figs 3 and 4). We use the radio luminosity ($S_{\rm rad,16}D^2$) results calculated by subtracting the predicted greybody contribution at 16 GHz ($S_{\rm gb,16}$) from the measured flux density ($S_{\rm 16\,GHz}$), in the correlations that follow to ensure that the values used are representative of only the outflow component of the radio emission. We compare the correlations between both SED scenarios and examine the relation of this sample to existing correlations.

6.6.1 *Note on classification*

AMI Consortium: Scaife et al. (2011b) found that when comparing bolometric temperatures determined using *IRAS* data (Hatchell et al. 2007a) and those found from fluxes calculated using *Spitzer* SEDs (Dunham et al. 2008), the *IRAS* temperatures were, on average, a factor of 1.6 higher than the corresponding *Spitzer* values. Bolometric temperature is one of the indicators for protostellar class and

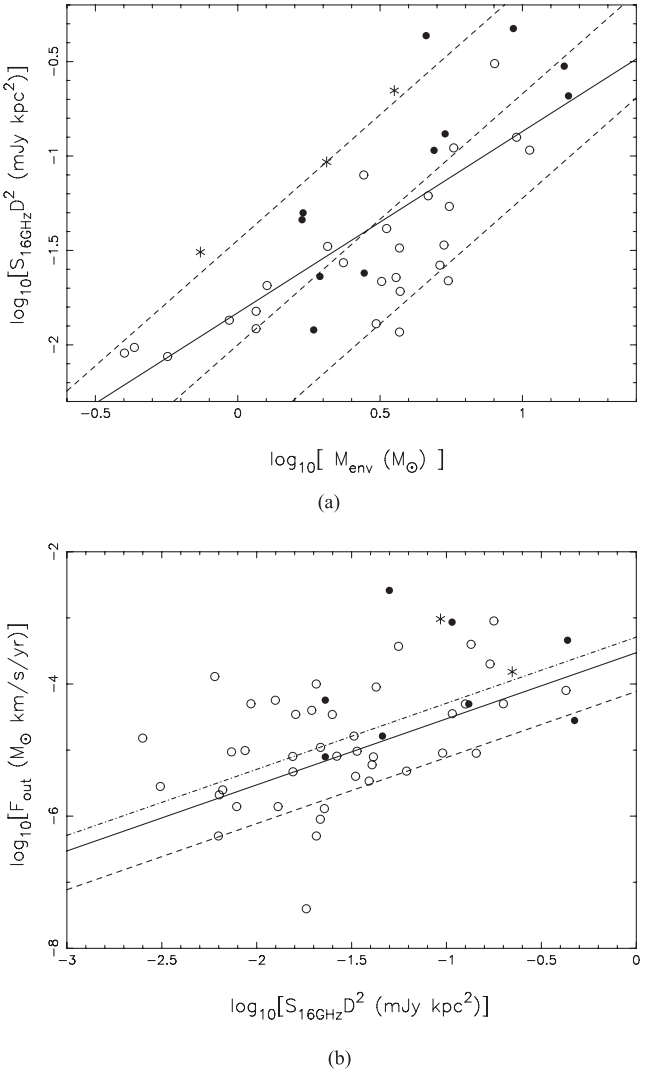

Figure 4. (a) Correlation of envelope mass with 1.9 cm radio luminosity, where the solid line indicates the best-fitting correlation using the combined data set (see Section 6.6.3), the dashed lines indicate a slope of 1.33 and the 1σ limits on the distribution of data relative to this slope (see AMI Consortium: Scaife et al. 2011b); (b) correlation of 1.9 cm radio luminosity with outflow force. Filled circles represent Class 0 sources from this sample, stars are Class I, and unfilled circles are previous data. The solid line indicates the shock ionization model of Curiel et al. (1989) with a temperature of $T_e = 10^4$ K. The upper (lower) dashed line indicates the same model with a temperature of $T_e = 3000$ K (10^5 K; AMI Consortium: Scaife et al. 2011b).

within this sample, one of the sources with $70 \leq T_{bol} \leq 150$ (HH 111) will change from Class I to 0 when the *Spitzer* temperature is used.

6.6.2 Correlation with bolometric luminosity

Fig. 3 shows the correlation of radio luminosity with bolometric luminosity for (a) Scenario (i), where T_d is fixed, and (b) Scenario (ii), where T_d varies. These new data extend the trend into higher luminosities. We note that the bolometric luminosity for the Serpens MMS 1 source used here is $L_{bol} = 17.3\,L_\odot$ (Enoch et al. 2009a); however significantly higher luminosities have been reported for this object in the literature which could explain the offset from the trend (see Section 5.9). The value of α' is unconstrained for HH 26 IR due to insufficient low-frequency data. As a result, our method calculates a significant value for $S_{gb,16}$, resulting in a value of $S_{rad,16}D^2$ consistent with zero due to the low flux density detected by AMI. HH 26 IR is therefore not included in the plots. Data below 8 GHz are needed to constrain the spectral index of this source and establish an accurate measure of the radio luminosity.

Two sources, L1551 NE and HH 25 MMS, have their location change significantly between Figs 3(a) and (b), due to the large difference in their radio luminosities between the two SED scenarios (as discussed extensively in Section 6). Larger radio luminosities were calculated for both sources in the case where T_d is fixed. However, the lower radio luminosity calculated from the scenario where T_d is allowed to vary for HH 25 MMS is in better agreement with the trend than the higher value from the scenario where T_d is fixed. The opposite is true for L1551 NE, and the radio luminosity calculated for this source from Scenario (i) is in better agreement with the trend than the one calculated from Scenario (ii). Like HH 26 IR, L1551 NE deviates from the trend due to a radio luminosity $S_{rad,16}D^2 \approx 0$ when T_d varies, and more observations at these frequencies are needed to constrain the spectral index and establish the radio luminosity.

We use a two-sample Kolmogorov–Smirnov (KS) test to determine whether the sample from this paper is consistent with the known correlation. We reject the null hypothesis of no difference between the data sets if the probability is less than the standard cut-off value of p=0.05. We find p-values of p=0.021 and =0.037 for Scenarios (i) and (ii), respectively, indicating that the sample from this work is statistically different from the previous sample in both scenarios.

We attribute this discrepancy to the values of the bolometric luminosity, rather than the radio luminosity, as no similar effect is seen in the correlation with envelope mass (see Section 6.6.3). There are a number of possible explanations. The data set from previous papers (open circles in Fig. 3) has bolometric luminosity values dominated by a single catalogue (Hatchell et al. 2007a), whereas the current sample has values from a much wider range of references. We might therefore expect a larger degree of scatter in the current data set due to differences in methodology. Alternatively, it is possible that the bolometric luminosities derived in Hatchell et al. (2007a) which dominate the archival data set have themselves a systematic offset from those found more generally in the literature; however this seems unlikely as it has not been noted in previous comparisons. A further possibility is that the current sample is (on average) biased towards sources with high ratios of bolometric luminosity to envelope mass. Since these sources are preferentially selected to be well-known radio protostars it is likely that this effect is present at some level. We therefore suggest that the underlying cause of the discrepancy is a combination of both this last possibility and the first.

6.6.3 Correlation with envelope mass

Fig. 4(a) shows the correlation between radio luminosity and envelope mass. The envelope masses listed in Column 8 of Table 3 were determined using the 850 μm flux density from the Fundamental Map Object Catalogue (di Francesco et al. 2008) in the following way:

$$M_{env} = \frac{S_\nu D^2}{\kappa_\nu B_\nu(T_d)}, \quad (6)$$

where κ_ν is the opacity index, $B_\nu(T_d)$ is the Planck function at a dust temperature T_d and the scaling factor $[\kappa_\nu B_\nu(T_d)]^{-1}$ uses the scaled

value from Hatchell et al. (2007a), applied in AMI Consortium: Scaife et al. (2012b). This fixes us on the same scale as Enoch et al. (2009a) and allows for comparisons between the data sets. Distances used are listed in Column 3 of Table 3. Froebrich (2005) find that lower dust temperature of 15 K, e.g., as suggested by Motte & André (2001) and Hatchell et al. (2007a), would lead to envelope masses that are a factor of 1.6 higher; however this should not affect our results as we are maintaining consistency within our sample. The SCUBA (di Francesco et al. 2008) 850 μm flux density is unresolved for NGC 1333 *IRAS* 2A and B, and so we use the values from Enoch et al. (2009b) for these objects.

The data from this paper are combined with those from AMI Consortium: Scaife et al. (2011a, 2011b) to examine the correlation of radio luminosity with envelope mass. It can be seen from Fig. 4(a) that the data from this work are consistent with those from the literature. A best-fitting correlation using the combined data set is found to be

$$\log[L_{\rm rad}({\rm mJy\,kpc^2})] = (-1.83 \pm 0.25) + (0.96 \pm 0.41)\log[M_{\rm env}({\rm M}_\odot)].$$

Following AMI Consortium: Scaife et al. (2011b) we also compare the data to a power law with index 1.33, shown as a dashed line in Fig. 4(a). We note that the fitted correlation is consistent with this index at the 1σ level.

Class I sources are expected to have smaller envelope masses than Class 0 by definition (see Section 1) but from these data there is no evident deviation from the trend based on evolutionary class. In fact, the Class I sources in this sample are all found along the $+1\sigma$ level line of the correlation.

From the KS test we find p-values of p=0.374 and p=0.54 for Scenarios (i) and (ii), respectively, indicating that the sample from this work is consistent with the correlations found from the previous sample in both scenarios.

Observational bias in the $L_{\rm rad}$–$M_{\rm env}$ correlation We note that the correlation fitted directly to the data shown in Fig. 4 will be subject to an observational bias due to the low significance end of the data. This form of Eddington bias causes the slope of the fitted correlation to be artificially shallow due to the increased data scattered above the correlation, relative to that scattered below the correlation which will be missed due to the detection limit. Such a bias can be corrected statistically, and following the method of Herranz et al. (2006) we use a maximum likelihood estimator for the slope, m, to recover a value of $\hat{m} = 1.01$.

The correlation with bolometric luminosity will also be subject to a similar bias. However, we do not correct the fit in this case as the detection limit is not the only criterion for detection of a radio counterpart in this case, as shown in AMI Consortium: Scaife et al. (2011b).

6.6.4 Correlation with outflow force

The 1.9 cm radio luminosity data presented here are consistent with the loose correlation with outflow force measured in AMI Consortium: Scaife et al. (2011a, 2011b) (see Fig. 4b). As discussed in AMI Consortium: Scaife et al. (2011a), the lack of a well-defined correlation in this case may by due to the errors inherent in measurements of outflow force. Class 0 objects are generally considered to have more energetic outflows than Class I, but there is no clear evolutionary division in the correlation presented here.

Many studies increase their outflow forces by a factor of 10 to account for optical depth and inclination effects, following Bontemps et al. (1996). From the current sample, only two the values for outflow force from the literature have been corrected in this way: L1527 and Serpens MMS (see Table 3). As the majority of the data included in Fig. 4(b) have this correction implemented, we apply the same adjustment to the values in Table 3 for the purposes of the plot.

6.7 Variability

Radio variability might be expected for Class 0 and I sources due to episodic accretion rates and mass ejection in the outflows (Kenyon & Hartmann 1995; Young & Evans 2005). However, only two sources, L1551 IRS 5 and Serpens SMM 1, show strong signs of variability based on examination of their SEDs (see Figs. B1 and B2). This could be due to the fact that there is a comparatively larger amount of archival data for these sources, and it is likely that a majority of the sources in this sample possess variable natures but more observations at multiple epochs are needed to confirm this. In the case of NGC 2264 G, evidence for variability has been shown (Gómez et al. 1994) for an object in the same region as the driving source of this outflow which will affect the results of unresolved data.

L1551. Rodríguez et al. (2003a) have compiled measurements of L1551 IRS 5 at 2 cm from 1983 to 1998 to determine the proper motion of the multiple sources, and by comparing different epochs they found that the southern component underwent a major ejection event during the late 1980s and showed considerable elongation in the E–W direction. By comparing data at 5 and 15 GHz taken at different epochs (see Appendix C), there is clear evidence of variability. The flux densities measured at 5 GHz range by a factor of ≈1.7 over all epochs, while the flux densities measured at 15 GHz range by a factor of ≈2.2. In addition, the VLA observations of Keene & Masson (1990) were measured in 1988 September, and their flux density at 15 GHz is a factor of ≈1.7 higher than the flux density measured in this work at a similar frequency. Lim & Takakuwa (2006) detect three circumstellar dust discs in this region, and therefore luminosity variations might be expected. These authors have discussed that the flux of the N jet (see Section 5 in this work) is typically higher than the flux of the S jet, except during the epoch of the major ejection event of the southern jet.

Serpens. Evidence for variability has been shown for Serpens SMM 1 by AMI Consortium: Scaife et al. (2012b) and references therein. Curiel et al. (1993) suggest that the knotty structure in the NW and SE components is the result of a discrete ejection of material ('bullets') from the source, which could account for the radio flare event in the archival data (AMI Consortium: Scaife et al. 2012b) that appear to have faded. The observations at 1.9 cm for SMM 1 presented in this work were taken on 2011 October 11 and the flux density (see Table 5) is a factor of ≈1.5 higher than that presented in AMI Consortium: Scaife et al. (2012b) who measure a flux density of 4.736 ± 0.237 at 1.8 cm from observations taken between 2010 December and 2011 January. Our measured flux density is within the uncertainty limits of the 15 GHz flux density of 10 ± 3 mJy found by Snell & Bally (1986). Enoch et al. (2009a) detect a high-mass disc around this source which should be unstable and therefore exhibit luminosity variations.

HH 1. The Herbig–Haro object HH 1 has been previously detected at centimetre wavelengths (e.g. Rodríguez et al. 1990, 2000); however, here we do not detect HH 1 at 1.9 cm. We calculate a flux density upper limit of 0.34 mJy for this object, inconsistent with the value of 0.78 mJy at 2 cm found by Rodríguez et al. (1990). However, Pravdo et al. (1985) also failed to detect HH 1 in the radio, suggesting that this source is variable. Indeed, multi-wavelength

observations of this object have been discussed by Raga et al. (2011), and HH 1 has been shown to be variable at radio wavelengths. Future observations with the AMI and eMERLIN at the same epoch will provide a better picture of the variability of these objects.

7 CONCLUSIONS

We have presented 16 GHz observations made with AMI of a sample of low-mass young stars driving jets.

(i) The data presented in this work provide support for free–free emission as the dominant mechanism for producing the radio luminosity from these YSOs. Across the AMI channel bands 80 per cent of the detected protostellar sources in the target sample have spectral indices $-0.1 \leq \alpha_{\rm AMI} \leq 2$ consistent with free–free emission, and we find an average spectral index $\overline{\alpha_{\rm AMI}} = 0.42 \pm 0.59$. Although the flux densities integrated over the whole of the source are in general indicative of free–free emission, it could be possible that subcomponents within the source show non-thermal (i.e. negative) spectra.

(ii) We have also presented and examined SEDs for each detected protostellar source, combining the AMI data with available archival data from an extensive literature search. We tested two scenarios to obtain maximum likelihood values for the spectral indices, dust opacity indices and dust temperatures. In Scenario (i) we fix $T_{\rm d}$ for each source based on protostellar evolutionary class and find that 80 per cent of the objects in the target sample have spectral indices consistent with free–free emission, and we calculate an average spectral index $\overline{\alpha'} = 0.20 \pm 0.41$ consistent with the value for a well-collimated outflow. In Scenario (ii) we do not fix $T_{\rm d}$, and we find the same average value for the spectral index. These values for the spectral indices are consistent with expectations as all target sources have known outflows.

(iii) We examine the errors associated with determining the radio luminosity and find that the dominant source of error is the uncertainty on β.

(iv) In both scenarios we find that NGC 2264 G and L723 have $\alpha' \leq -0.1$, inconsistent with free–free emission. For these two sources there are other objects within close proximity (i.e. within the synthesized beam) that have non-thermal spectral indices that affect the integrated flux densities. Higher spatial resolution data can help constrain the emission mechanism for the driving sources of these outflows. We also find $\alpha' > 2$ in some cases (e.g. NGC 1333 *IRAS* 2A) suggesting that the lower frequency data are an extension of the greybody emission and that there is no free–free component detectable in these data.

(v) We examine correlations between the radio luminosity and bolometric luminosity, envelope mass, and outflow force and find that these data are broadly consistent with correlations found by previous samples. We find a slight bias in the correlation with bolometric luminosity towards higher values of $L_{\rm bol}$.

(vi) Evidence for variability has been shown for L1551 IRS 5 and Serpens SMM 1 by close inspection of their SEDs. It is apparent from their histories that they have undergone radio flare events, supporting non-steady accretion accretion models of protostellar evolution. We also find variability in the Herbig–Haro object HH 1.

ACKNOWLEDGMENTS

We thank the staff of the Lord's Bridge Observatory for their invaluable assistance in the commissioning and operation of the AMI. The AMI is supported by Cambridge University and the STFC. We thank the anonymous referee for their careful and constructive reading of our paper. RA would like to acknowledge support from Science Foundation Ireland under grant 11/RFP/AST3331.

REFERENCES

Altenhoff W. J., Thum C., Wendker H. J., 1994, A&A, 281, 161
AMI Consortium: Davies M. L. et al., 2011, MNRAS, 415, 2708
AMI Consortium: Scaife A. M. M. et al., 2011a, MNRAS, 410, 2662
AMI Consortium: Scaife A. M. M. et al., 2011b, MNRAS, 415, 893
AMI Consortium: Scaife A. M. M. et al., 2012a, MNRAS, 420, 3334
AMI Consortium: Scaife A. M. M. et al., 2012b, MNRAS, 420, 1019
AMI Consortium: Zwart J. T. L. et al., 2008, MNRAS, 391, 1545
André P., Ward-Thompson D., Barsony M., 1993, ApJ, 406, 122
André P., Ward-Thompson D., Barsony M., 2000, Protostars and Planets IV, p. 59
Andrews S. M., Williams J. P., 2005, ApJ, 631, 1134
Anglada G., 1995, Rev. Mex. Astron. Astrofis. Conf. Ser., 1, 67
Anglada G., Estalella R., Rodríguez L. F., Torrelles J. M., Lopez R., Canto J., 1991, ApJ, 376, 615
Anglada G., Rodríguez L. F., Torrelles J. M., 1996, ApJ, 473, L123
Anglada G., Villuendas E., Estalella R., Beltrán M. T., Rodríguez L. F., Torrelles J. M., Curiel S., 1998, AJ, 116, 2953
Anglada G., Rodríguez L. F., Osorio M., Torrelles J. M., Estalella R., Beltrán M. T., Ho P. T. P., 2004, ApJ, 605, L137
Antoniucci S., Nisini B., Giannini T., Lorenzetti D., 2008, A&A, 479, 503
Bachiller R., Martin-Pintado J., Tafalla M., Cernicharo J., Lazareff B., 1990, A&A, 231, 174
Bachiller R., Andre P., Cabrit S., 1991, A&A, 241, L43
Bachiller R., Guilloteau S., Dutrey A., Planesas P., Martin-Pintado J., 1995, A&A, 299, 857
Bally J., Devine D., Alten V., Sutherland R. S., 1997, ApJ, 478, 603
Barsony M., Chandler C. J., 1993, ApJ, 406, L71
Barsony M., Ward-Thompson D., André P., O'Linger J., 1998, ApJ, 509, 733
Beltrán M. T., Estalella R., Anglada G., Rodríguez L. F., Torrelles J. M., 2001, AJ, 121, 1556
Bieging J. H., Cohen M., 1985, ApJ, 289, L5
Bieging J. H., Cohen M., Schwartz P. R., 1984, ApJ, 282, 699
Bontemps S., Andre P., Ward-Thompson D., 1995, A&A, 297, 98
Bontemps S., André P., Terebey S., Cabrit S., 1996, A&A, 311, 858
Cabrit S., Andre P., 1991, ApJ, 379, L25
Caratti o Garatti A., Giannini T., Nisini B., Lorenzetti D., 2006, A&A, 449, 1077
Carkner L., Mamajek E., Feigelson E., Neuhauser R., Wichmann R., Krautter J., 1997, ApJ, 490, 735
Carrasco-González C., Anglada G., Rodríguez L. F., Torrelles J. M., Osorio M., Girart J. M., 2008, ApJ, 676, 1073
Carrasco-González C., Rodríguez L. F., Anglada G., Martí J., Torrelles J. M., Osorio M., 2010a, Sci, 330, 1209
Carrasco-González C., Rodríguez L. F., Torrelles J. M., Anglada G., González-Martín O., 2010b, AJ, 139, 2433
Casali M. M., Eiroa C., Duncan W. D., 1993, A&A, 275, 195
Chandler C. J., Richer J. S., 2000, ApJ, 530, 851
Chen H., Myers P. C., Ladd E. F., Wood D. O. S., 1995, ApJ, 445, 377
Chen X., Launhardt R., Henning T., 2009, ApJ, 691, 1729
Choi M., 2009, ApJ, 705, 1730
Cohen M., Bieging J. H., Schwartz P. R., 1982, ApJ, 253, 707
Condon J. J., Cotton W. D., Greisen E. W., Yin Q. F., Perley R. A., Taylor G. B., Broderick J. J., 1998, AJ, 115, 1693
Curiel S., Rodriguez L. F., Bohigas J., Roth M., Canto J., Torrelles J. M., 1989, Astrophys. Lett. Commun., 27, 299
Curiel S., Raymond J. C., Moran J. M., Rodríguez L. F., Canto J., 1990, ApJ, 365, L85
Curiel S., Rodríguez L. F., Moran J. M., Canto J., 1993, ApJ, 415, 191
Curiel S., Torrelles J. M., Rodríguez L. F., Gómez J. F., Anglada G., 1999, ApJ, 527, 310

Davis C. J., Smith M. D., 1995, ApJ, 443, L41
Davis C. J., Ray T. P., Eisloeffel J., Corcoran D., 1997, A&A, 324, 263
Davis C. J., Matthews H. E., Ray T. P., Dent W. R. F., Richer J. S., 1999, MNRAS, 309, 141
de Zotti G., Ricci R., Mesa D., Silva L., Mazzotta P., Toffolatti L., González-Nuevo J., 2005, A&A, 431, 893
Dent W. R. F., Matthews H. E., Ward-Thompson D., 1998, MNRAS, 301, 1049
Devine D., Reipurth B., Bally J., 1999, AJ, 118, 972
di Francesco J., Johnstone D., Kirk H., MacKenzie T., Ledwosinska E., 2008, ApJS, 175, 277
Duarte-Cabral A., Fuller G. A., Peretto N., Hatchell J., Ladd E. F., Buckle J., Richer J., Graves S. F., 2010, A&A, 519, A27
Duncan R. A., Forster J. R., Gardner F. F., Whiteoak J. B., 1987, MNRAS, 224, 721
Dunham M. M., Crapsi A., Evans N. J., II, Bourke T. L., Huard T. L., Myers P. C., Kauffmann J., 2008, ApJS, 179, 249
Eiroa C., Torrelles J. M., Curiel S., Djupvik A. A., 2005, AJ, 130, 643
Emerson J. P., Harris S., Jennings R. E., Beichman C. A., Baud B., Beintema D. A., Wesselius P. R., Marsden P. L., 1984, ApJ, 278, L49
Enoch M. L. et al., 2006, ApJ, 638, 293
Enoch M. L., Corder S., Dunham M. M., Duchêne G., 2009a, ApJ, 707, 103
Enoch M. L., Evans N. J., II, Sargent A. I., Glenn J., 2009b, ApJ, 692, 973
Evans N. J., II, Levreault R. M., Beckwith S., Skrutskie M., 1987, ApJ, 320, 364
Feigelson E. D., Carkner L., Wilking B. A., 1998, ApJ, 494, L215
Fischer W. J. et al., 2010, A&A, 518, L122
Froebrich D., 2005, ApJS, 156, 169
Gezari D. Y., Pitts P. S., Schmitz M., 1999, VizieR Online Data Catalog, 2225, 0
Gibb A. G., 1999, MNRAS, 304, 1
Gibb A. G., Heaton B. D., 1993, A&A, 276, 511
Girart J. M., Estalella R., Anglada G., Torrelles J. M., Ho P. T. P., Rodríguez L. F., 1997, ApJ, 489, 734
Gomez J. F., Torrelles J. M., Ho P. T. P., Rodríguez L. F., Canto J., 1993, ApJ, 414, 333
Gómez J. F., Curiel S., Torrelles J. M., Rodríguez L. F., Anglada G., Girart J. M., 1994, ApJ, 436, 749
Gomez M., Whitney B. A., Kenyon S. J., 1997, AJ, 114, 1138
Gramajo L. V., Whitney B. A., Gómez M., Robitaille T. P., 2010, AJ, 139, 2504
Graves S. F. et al., 2010, MNRAS, 409, 1412
Gredel R., Reipurth B., 1994, A&A, 289, L19
Guilloteau S., Bachiller R., Fuente A., Lucas R., 1992, A&A, 265, L49
Hatchell J., Fuller G. A., Richer J. S., Harries T. J., Ladd E. F., 2007a, A&A, 468, 1009
Hatchell J., Fuller G. A., Richer J. S., 2007b, A&A, 472, 187
Herranz D., Sanz J. L., Lopez-Caniego M., Gonzalez-Nuevo J., 2006, in 2006 IEEE Int. Symp. Signal Processing and Information-Technology, Vol. 1, p. 541
Hobson M. P., Baldwin J. E., 2004, Appl. Optics, 43, 2651
Hogerheijde M. R., van Dishoeck E. F., Salverda J. M., Blake G. A., 1999, ApJ, 513, 350
Hurt R. L., Barsony M., 1996, ApJ, 460, L45
Jennings R. E., Cameron D. H. M., Cudlip W., Hirst C. J., 1987, MNRAS, 226, 461
Jørgensen J. K., Hogerheijde M. R., van Dishoeck E. F., Blake G. A., Schöier F. L., 2004, A&A, 413, 993
Jørgensen J. K., van Dishoeck E. F., Visser R., Bourke T. L., Wilner D. J., Lommen D., Hogerheijde M. R., Myers P. C., 2009, A&A, 507, 861
Keene J. B., Masson C. R., 1986, BAAS, 18, 973
Keene J., Masson C. R., 1990, ApJ, 355, 635
Kenyon S. J., Hartmann L., 1995, ApJS, 101, 117
Kenyon S. J., Dobrzycka D., Hartmann L., 1994, AJ, 108, 1872
Kirk H., Johnstone D., Tafalla M., 2007, ApJ, 668, 1042
Kun M., Balog Z., Kenyon S. J., Mamajek E. E., Gutermuth R. A., 2009, ApJS, 185, 451
Lada C. J., 1987, in Peimbert M., Jugaku J., eds, IAU Symp. Vol. 115, Star Forming Regions, p. 1
Lada C. J., Fich M., 1996, ApJ, 459, 638
Lee C.-F., Mundy L. G., Stone J. M., Ostriker E. C., 2002, ApJ, 576, 294
Lim J., Takakuwa S., 2006, ApJ, 653, 425
Lis D. C., Menten K. M., Zylka R., 1999, ApJ, 527, 856
Loinard L., Rodríguez L. F., D'Alessio P., Wilner D. J., Ho P. T. P., 2002, ApJ, 581, L109
Looney L. W., Mundy L. G., Welch W. J., 2000, ApJ, 529, 477
McMullin J. P., Mundy L. G., Wilking B. A., Hezel T., Blake G. A., 1994, ApJ, 424, 222
Margulis M., Lada C. J., 1986, ApJ, 309, L87
Margulis M., Lada C. J., Snell R. L., 1988, ApJ, 333, 316
Meehan L. S. G., Wilking B. A., Claussen M. J., Mundy L. G., Wootten A., 1998, AJ, 115, 1599
Melis C. et al., 2011, ApJ, 739, L7
Menten K. M., Reid M. J., Forbrich J., Brunthaler A., 2007, A&A, 474, 515
Morgan J. A., Snell R. L., Strom K. M., 1990, ApJ, 362, 274
Moriarty-Schieven G. H., Butner H. M., Wannier P. G., 1995, ApJ, 445, L55
Moriarty-Schieven G. H., Powers J. A., Butner H. M., Wannier P. G., Keene J., 2000, ApJ, 533, L143
Moriarty-Schieven G. H., Johnstone D., Bally J., Jenness T., 2006, ApJ, 645, 357
Motte F., André P., 2001, A&A, 365, 440
Nisini B., Giannini T., Lorenzetti D., 2002, ApJ, 574, 246
Nutter D., Ward-Thompson D., 2007, MNRAS, 374, 1413
Ohashi N., Kawabe R., Ishiguro M., Hayashi M., 1991, AJ, 102, 2054
Ohashi N., Hayashi M., Ho P. T. P., Momose M., 1997, ApJ, 475, 211
Phillips R. R., Gibb A. G., Little L. T., 2001, MNRAS, 326, 927
Pravdo S. H., Rodríguez L. F., Curiel S., Canto J., Torrelles J. M., Becker R. H., Sellgren K., 1985, ApJ, 293, L35
Raga A. C., Reipurth B., Cantó J., Sierra-Flores M. M., Guzmán M. V., 2011, Rev. Mex. Astron. Astrofis., 47, 425
Ray T. P., Muxlow T. W. B., Axon D. J., Brown A., Corcoran D., Dyson J., Mundt R., 1997, Nat, 385, 415
Reipurth B., 1989, Nat, 340, 42
Reipurth B., Raga A. C., Heathcote S., 1992, ApJ, 392, 145
Reipurth B., Chini R., Krugel E., Kreysa E., Sievers A., 1993, A&A, 273, 221
Reipurth B., Bally J., Devine D., 1997, AJ, 114, 2708
Reipurth B., Yu K. C., Rodríguez L. F., Heathcote S., Bally J., 1999, A&A, 352, L83
Reipurth B., Rodríguez L. F., Anglada G., Bally J., 2002, AJ, 124, 1045
Reipurth B., Rodríguez L. F., Anglada G., Bally J., 2004a, AJ, 127, 1736
Reipurth B., Rodríguez L. F., Anglada G., Bally J., 2004b, AJ, 127, 1736
Reynolds S. P., 1986, ApJ, 304, 713
Rodríguez L. F., 1995, Rev. Mex. Astron. Astrofis. Conf. Ser., 1, 1
Rodríguez L. F., 1998, Rev. Mex. Astron. Astrofis. Conf. Ser., 7, 14
Rodríguez L. F., Curiel S., 1989, Rev. Mex. Astron. Astrofis., 17, 115
Rodriguez L. F., Reipurth B., 1994, A&A, 281, 882
Rodríguez L. F., Reipurth B., 1998, Rev. Mex. Astron. Astrofis., 34, 13
Rodríguez L. F., Canto J., Torrelles J. M., Ho P. T. P., 1986, ApJ, 301, L25
Rodríguez L. F., Canto J., Mirabel I. F., Ruiz A., 1989a, ApJ, 337, 712
Rodríguez L. F., Curiel S., Moran J. M., Mirabel I. F., Roth M., Garay G., 1989b, ApJ, 346, L85
Rodríguez L. F., Ho P. T. P., Torrelles J. M., Curiel S., Canto J., 1990, ApJ, 352, 645
Rodríguez L. F., Anglada G., Curiel S., 1997, ApJ, 480, L125
Rodríguez L. F., Anglada G., Curiel S., 1999, ApJS, 125, 427
Rodríguez L. F., Delgado Arellano V. G., Gómez Y., Reipurth B., Torrelles J. M., Noriega-Crespo A., Raga A. C., Cantó J., 2000, AJ, 119, 882
Rodríguez L. F., Curiel S., Cantó J., Loinard L., Raga A. C., Torrelles J. M., 2003a, ApJ, 583, 330
Rodríguez L. F., Porras A., Claussen M. J., Curiel S., Wilner D. J., Ho P. T. P., 2003b, ApJ, 586, L137
Rodríguez L. F., Moran J. M., Franco-Hernández R., Garay G., Brooks K. J., Mardones D., 2008a, AJ, 135, 2370

Rodríguez L. F., Torrelles J. M., Anglada G., Reipurth B., 2008b, AJ, 136, 1852
Rosvick J. M., Davidge T. J., 1995, PASP, 107, 49
Sandell G., Knee L. B. G., Aspin C., Robson I. E., Russell A. P. G., 1994, A&A, 285, L1
Sato F., Fukui Y., 1989, ApJ, 343, 773
Schwartz P. R., Gee G., Huang Y.-L., 1988, ApJ, 327, 350
Shirley Y. L., Evans N. J., II, Rawlings J. M. C., Gregersen E. M., 2000, ApJS, 131, 249
Shirley Y. L., Evans N. J., II, Rawlings J. M. C., 2002, ApJ, 575, 337
Shirley Y. L., Mason B. S., Mangum J. G., Bolin D. E., Devlin M. J., Dicker S. R., Korngut P. M., 2011, AJ, 141, 39
Snell R. L., Bally J., 1986, ApJ, 303, 683
Snell R. L., Bally J., Strom S. E., Strom K. M., 1985, ApJ, 290, 587
Stapelfeldt K. R., Scoville N. Z., 1993, ApJ, 408, 239
Straižys V., Černis K., Bartašiūtė S., 1996, Baltic Astron., 5, 125
Terebey S., Padgett D. L., 1997, in Reipurth B., Bertout C., eds, IAU Symp. Vol. 182, Herbig–Haro Flows and the Birth of Stars, p. 507
Tobin J. J., Hartmann L., Loinard L., 2010, ApJ, 722, L12
Torrelles J. M., Ho P. T. P., Rodríguez L. F., Canto J., 1985, ApJ, 288, 595
van Kempen T. A. et al., 2009, A&A, 507, 1425
Ward-Thompson D., Eiroa C., Casali M. M., 1995, MNRAS, 273, L25
Wendker H. J., 1995, A&AS, 109, 177
Wilking B. A., Blackwell J. H., Mundy L. G., Howe J. E., 1989, ApJ, 345, 257
Wolf-Chase G. A., Barsony M., O'Linger J., 2000, AJ, 120, 1467
Wu J., Dunham M. M., Evans N. J., II, Bourke T. L., Young C. H., 2007, AJ, 133, 1560
Yang J., Ohashi N., Yan J., Liu C., Kaifu N., Kimura H., 1997, ApJ, 475, 683
Young C. H., Shirley Y. L., Evans N. J., II, Rawlings J. M. C., 2003, ApJS, 145, 111
Young C. H., Evans N. J., II, 2005, ApJ, 627, 293

APPENDIX A: AMI MAPS

Maps of each field are shown. AMI data are shown uncorrected for the primary beam response. The positions of known Class 0 and Class I objects are indicated as crosses (+) and stars (∗), respectively. The positions for those found in Perseus (L1448 and HH 7-11) are from Hatchell et al. (2007a), HH 1-2 from Fischer et al. (2010) and Serpens from Duarte-Cabral et al. (2010). Crosses (×) represent known sources of unknown evolutionary class. We plot the half power point of the primary beam as a solid circle (≈6 arcmin at 16 GHz) and the FWHM of the PSF as the filled ellipse in the bottom-left corner (see Table 1). Contours at 5, 10, 15, 20 $\sigma_{\rm rms}$ etc., where $\sigma_{\rm rms}$ values for each source are listed in Table 1.

APPENDIX B: SPECTRAL ENERGY DISTRIBUTIONS

The observed radio spectra over the AMI frequency channels 3–8 combined with flux densities from the literature. Maximum likelihood results from Scenario (ii) are overlaid (see Table 8). The list of archival data used in the SEDs can be found in Appendix C. Only data $\nu < 3$ THz ($\lambda > 100$ μm) were included in the fit, but *IRAS* data $\nu > 3$ THz are included in the plots for illustration.

APPENDIX C: SED REFERENCE TABLE

An extensive literature search was conducted for unresolved, integrated flux densities to include in the SEDs. It should be noted that Wendker (1995) was a useful reference. High-resolution data that were highly discrepant due to flux loss or data with high uncertainties (e.g. 450 μm data from di Francesco et al. 2008) were not included. Where uncertainties were not provided, an error of 10 per cent was used in the model fittings and this is indicated by the symbol dagger (†).

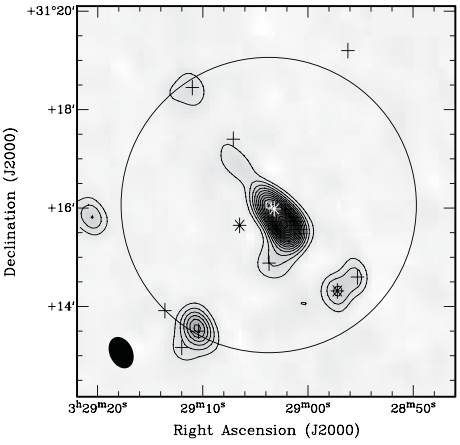

HH 7-11

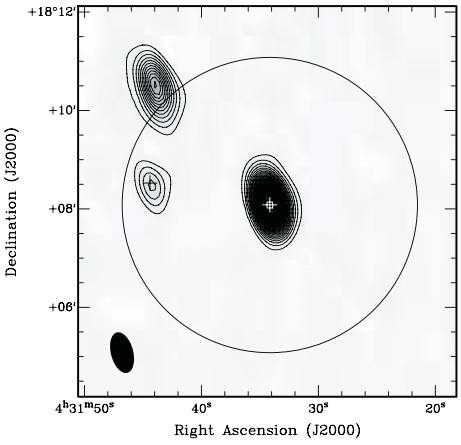

L1551

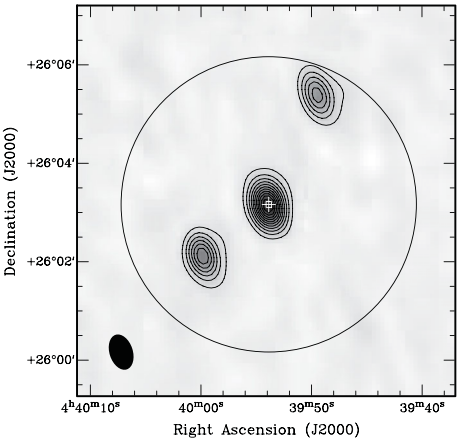

L1527

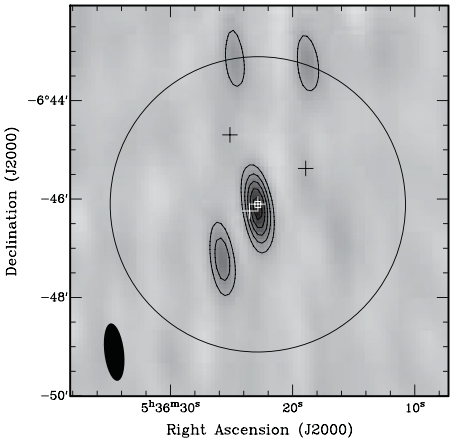

HH 1-2

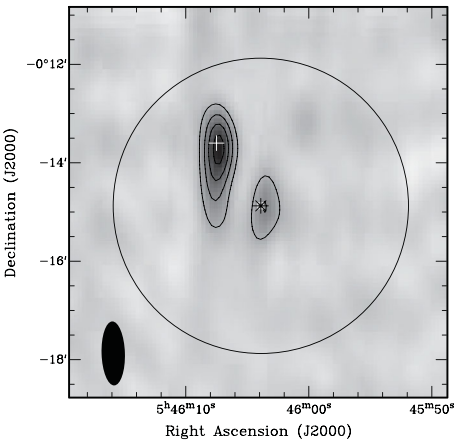

HH 26IR

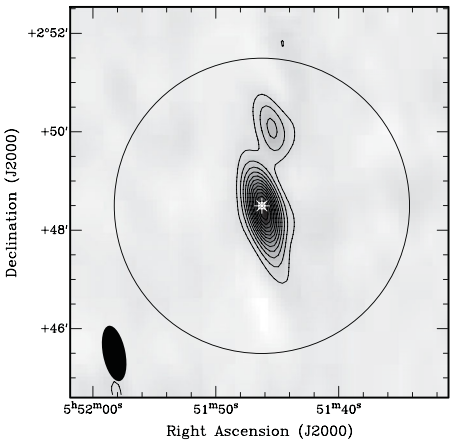

HH 111

Figure A1. The AMI 16 GHz combined-channel map for each source.

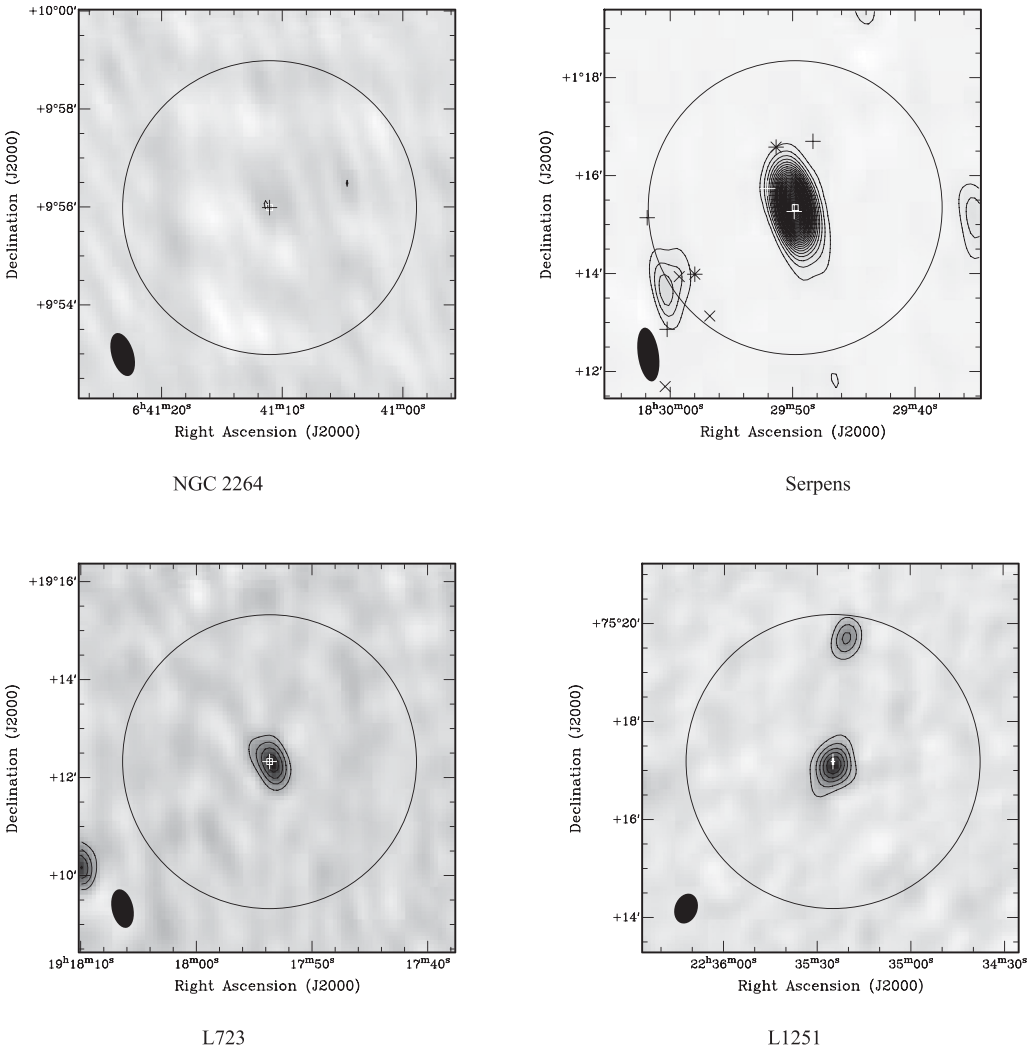

Figure A2. The AMI 16 GHz combined-channel map for each source – continued.

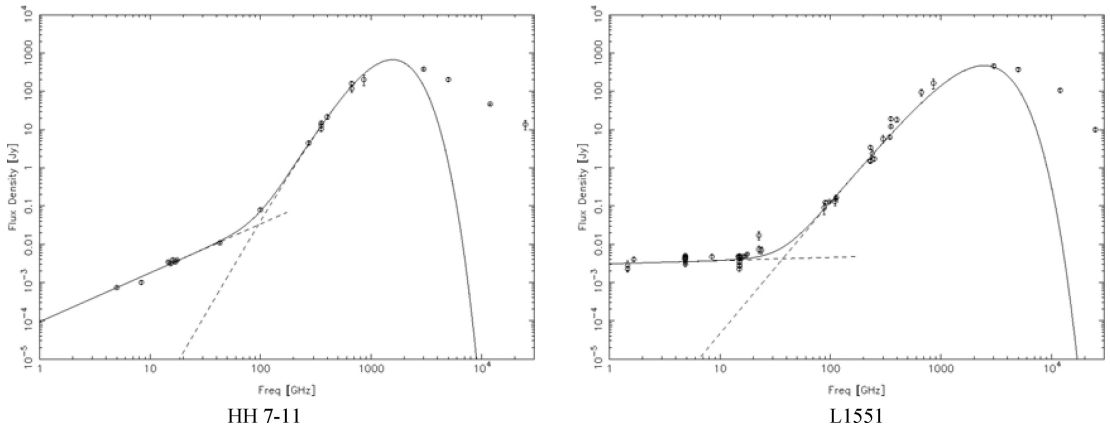

Figure B1. The SED for each source along with the model fit.

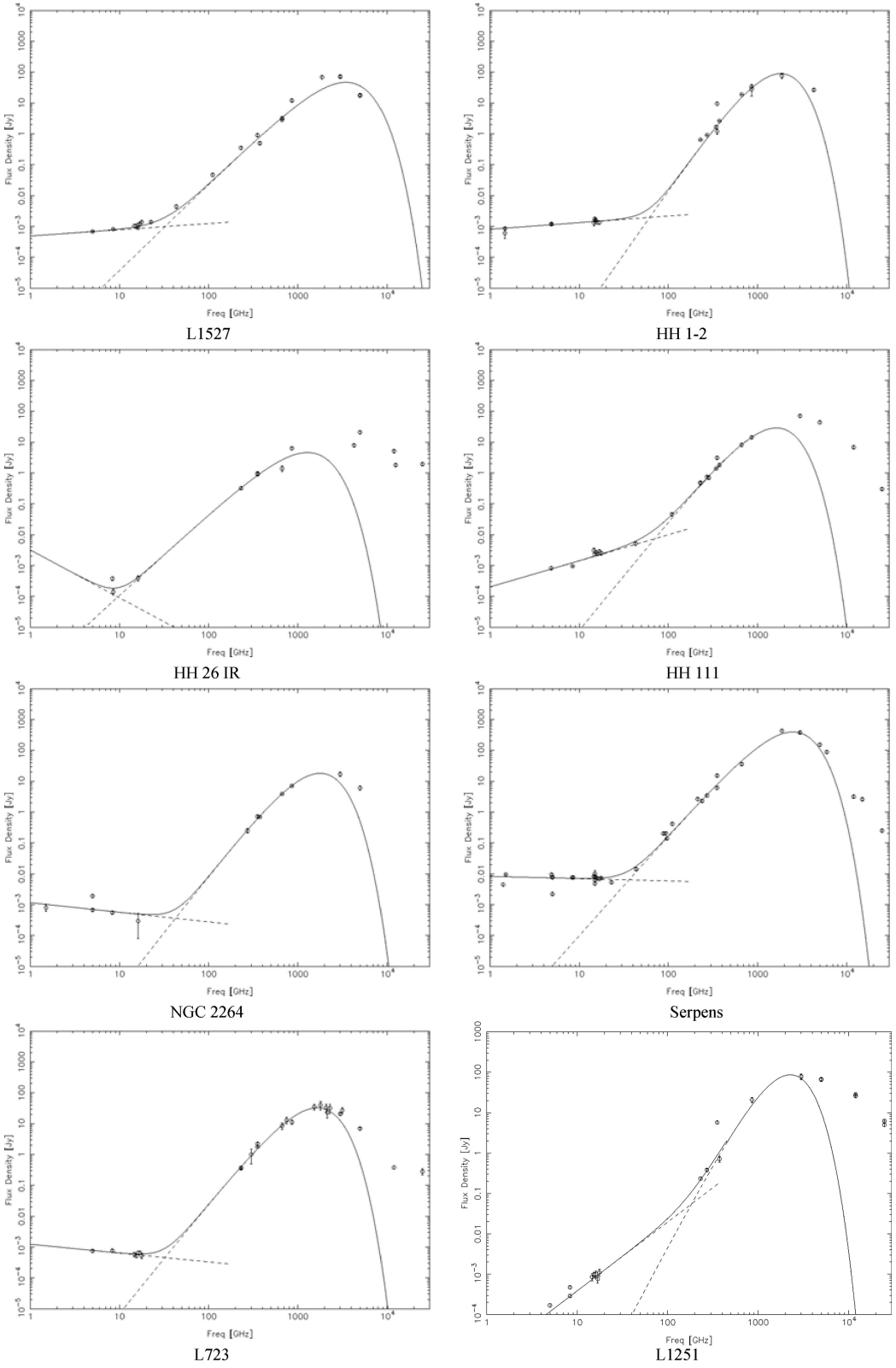

Figure B2. The SED for each source along with the model fit – continued.

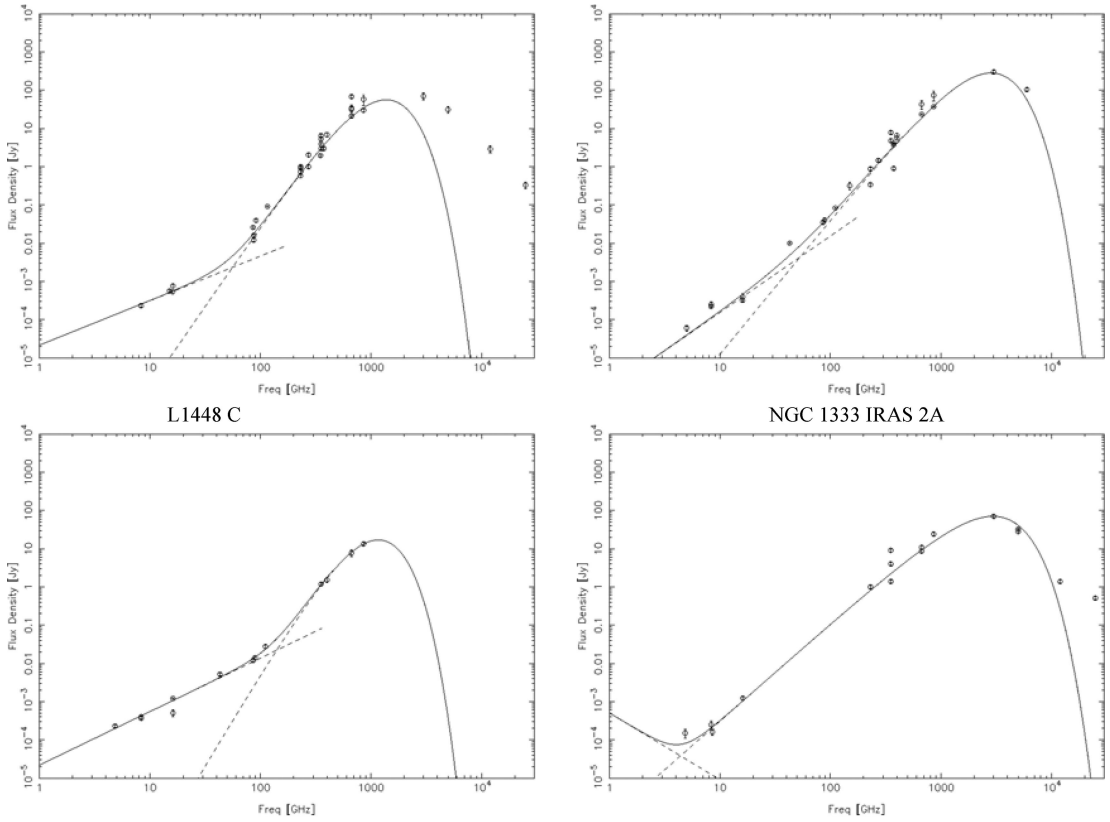

Figure B3. The SED for each source along with the model fit – continued.

SUPPORTING INFORMATION

Additional Supporting Information may be found in the online version of this article.

Tables C1– C7.

Please note: Wiley-Blackwell are not responsible for the content or functionality of any supporting materials supplied by the authors. Any queries (other than missing material) should be directed to the corresponding author for the article.

This paper has been typeset from a TEX/LATEX file prepared by the author.